Hyperfine Interaction of the Group IV Color Centers

By
Isaac B. W. Harris

B.A.Sc., University of Waterloo (2018)

Submitted to the Department of Electrical Engineering and Computer Science in partial fulfillment of the requirements for the degree of

Master of Science

at the

MASSACHUSETTS INSTITUTE OF TECHNOLOGY

September 2023

Authored by: Isaac B. W. Harris
Department of Electrical Engineering and Computer Science
June 14, 2023

Certified by: Dirk R. Englund
Professor of Electrical Engineering and Computer Science
Thesis Supervisor

Accepted by: Leslie A. Kolodziejski
Professor of Electrical Engineering and Computer Science
Chair, Department Committee on Graduate Students

Hyperfine Interaction of the Group IV Color Centers

by

Isaac B. W. Harris

Submitted to the Department of Electrical Engineering and Computer Science
on June 14, 2023, in partial fulfillment of the
requirements for the degree of
Master of Science

Abstract

The group IV-negative color centers (SiV^-, GeV^-, SnV^-) are one of the leading candidates for spin-photon interfaces for use in quantum information technologies. They feature highly coherent optical transitions, as well as native electron and nuclear spins that can be used as quantum memories. While the optical and electronic properties of these defects have been studied extensively in previous works, a detailed theory of the hyperfine coupling to the nuclear spin is lacking. This work presents a complete theoretical model of the hyperfine coupling to the intrinsic dopant nucleus in the group IV-negative color centers, complete with ab-initio theoretical predictions of the hyperfine coupling strength, and supported by experimental observation in an isotopically engineered sample. The theoretical model explains the observed hyperfine features well, providing a foundation for future work to use the intrinsic nuclear spin in quantum protocols.

Acknowledgments

I have a large number of people to thank for being able to (finally) complete this thesis. Firstly, my advisor, Dirk Englund, for providing a wealth of helpful ideas and advice. I would also like to thank lab mates in the Quantum Photonics Group: Kevin Chen, Ian Christen, Maddie Sutula, and many others, who helped prepare samples for this work and provided constant support for running the experiments for this and other work. The results in this thesis would not have been possible without the unique samples prepared through a joint effort with Element Six and Sandia National Labs. Additionally, the magneto-optic experiments in this thesis would not have been performed without our collaborators in Mete Atatüre's group at the University of Cambridge, who also provided wonderful feedback in our joint papers, and were incredibly welcoming when I was able to visit them in person.

Finally, I would like to thank my friends and family in Boston and elsewhere for giving me many excuses to get out of the dark lab on various adventures. My parents in particular have been incredibly supportive through all the ups and downs, and for that I am incredibly grateful.

Contents

List of Figures

List of Tables

Chapter 1

Introduction

Quantum technologies have attracted significant research efforts for their promised improvements over their classical counterparts in computation speed, communication security, and sensor performance. Despite extensive ongoing research efforts, significant scientific and engineering challenges remain before these technologies can be deployed in the real world. Spin photon interfaces are key components in several proposed and demonstrated quantum communication [20, 54, 77, 85], transduction [67, 79], sensing [86, 55, 30], and computing schemes [47, 21], and are one of the major areas of active development. In these systems, a spin acts as a local quantum memory, and is coupled to photons via an optical transition, allowing for the generation of spin-photon entanglement [19, 10].

While much effort has gone into characterizing the properties of these spin-photon interfaces, the quantum information protocols listed above also require ancillary quantum registers in order to free up the spin memory for spin-photon entanglement. Consistent coupling to the ancillary memory remains a central challenge for quantum technologies that require spin-photon interfaces. This thesis follows the work performed in [41] characterising the ancillary memory in the form of the intrinsic nuclear spin for a particular spin-photon interface, the group IV-color center in diamond. The introduction that follows motivates the choice of the group IV-color centers in diamond. Chapter 2 then reviews a theoretical model of the group IV-color center spin-photon interface. Chapters 3 and 4 outline the development of a first-

principles theoretical model for the ancillary hyperfine nuclear spin memory, and the experimental verification of this model.

1.1 Quantum Information with Spin-Photon Interfaces

Spin-photon interfaces have been demonstrated in numerous systems, including electrons trapped in quantum dots [9, 28], single trapped ions [49, 13], single and ensemble trapped neutral atoms [45, 81, 101], and ensembles of ions in solid state [24]. One of the most promising and well studied types of spin-photon interfaces are optically addressable single point defects in solid state materials, called color centers [6, 7]. The solid state nature of these defects facilitates integration in photonic nanostructures [98, 25, 102, 56, 44, 78] compared to other spin-photon interfaces, since they can be Incorporated directly into the material that forms the nanostructure. Direct integration into nanostructures gives several key advantages:

- Improved photonic collection efficiency [4], which increases the efficiency of readout and entangling protocols.

- Enhanced interaction with the electromagnetic field via integration with cavities [69], which can provide Purcell enhancement of the rate of emission, and opens access to cavity based entanglement schemes [85].

- Large-scale integration, allowing large numbers of emitters to be addressed within a single system on a chip [64, 98].

Of particular interest are color centers in diamond, which provide state-of-the-art optical and spin properties.

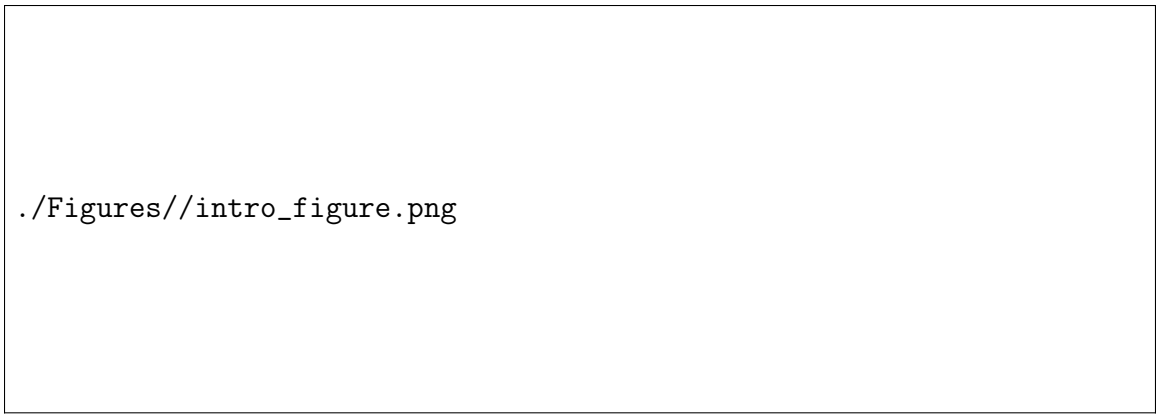

Figure 1-1: (a) Atomic structure of the NV^-, with carbon atoms in black, nitrogen in purple, and carbon vacancy in red. (b) Level structure of the NV^- showing the ground/excited S=1 triplet, and S=0 singlet manifolds. (c) Atomic structure of SiV^-, showing the silicon atom in blue. (d) Level structure of the SiV^- showing the effect of spin-orbit coupling that splits the four-fold degenerate $E_{g/u}$ levels into to pairs of two-fold degenerate levels by $\lambda_{g/u}$.

1.2 Color Centers in Diamond

1.2.1 Nitrogen Vacancy

The prototypical diamond color center is the negatively charged nitrogen-vacancy center, NV^-. This color center consists of a substitutional nitrogen atom positioned next to a vacancy in the diamond's carbon lattice, see Figure 1-1a. Electrons travelling through the diamond structure become trapped in orbitals localized around the dangling bonds of the nitrogen-vacancy defect, resulting in a spin-1 electronic ground state, with an excited manifold providing an optical transition, and intersystem crossing to a spin-0 manifold shown in Figure 1-1b.

Since nitrogen is already present as an impurity in most diamonds, the nitrogen vacancy is easily formed by annealing to allow vacancies to migrate to a location next to the nitrogen. In addition, the nitrogen-vacancy center's spin state can be initialized and read out at room temperature with off-resonant excitation due to intersystem crossing [39].

These attractive properties made the nitrogen-vacancy one of the pre-eminent spin-photon interfaces, with demonstrations of quantum sensing [55, 30], spin-photon

entanglement [54, 48], quantum networks [20, 17], and integration into nanocavities [64, 63]. However, in these later applications, the nitrogen-vacancy was found to be somewhat deficient. Due to its physical structure with C_{3v}-symmetry it lacks an inversion symmetry center, meaning it is sensitive to electric fields to first order. While this does not affect its ground state spin coherence, the electric field sensitivity means that the coherence of the optical transition is decreased in the presence of nearby charge traps [96, 22]. The result is an incoherent broadening of the optical transition that adversely affects the quality of spin-photon entanglement, an effect which is particularly severe when the color centers are embedded in photonic structures due to the proximity to charge traps at the structure's surface.

1.2.2 Group IV Vacancies

The problems with the nitrogen-vacancy's led to the search for other color centers in diamond that would exhibit better optical properties. A particularly prominent candidate to have emerged in recent years is the negatively charged silicon-vacancy center, SiV^-. This center has a very similar structure to the nitrogen-vacancy center, as shown in Figure 1-1c, however the larger size of the silicon atom means it is forced into an interstitial location in the diamond with D_{3d} -symmetry. The SiV^- therefore gains an inversion symmetry point, making it insensitive to electric field noise to first order, and it can be integrated into nanostructures with linewidths approaching the limit dictated by the optical lifetime of the excited state [84, 98]. Using this ability to integrate into nanophotonic structures, the SiV^- has been shown in a number of critical spin-photon interface demonstrations where strong spin-photon coupling is required [32, 69, 68, 59, 85]

The electronic structure of SiV^- shown in Figure 1-1d, is slightly changed compared to NV^-, with a spin-1/2 ground state that has an upper and lower branch due to a degeneracy of the orbital degree of freedom [66, 43]. The lack of intersystem crossing means that the spin state must be readout and initialized by resonantly pumping on an optical transition to move the population to the state with opposite spin [82, 76, 87]. In addition, the presence of the orbital degeneracy and spin-orbit coupling adds a

phonon-mediated decoherence mechanism to the spin degree of freedom [53]. This greatly reduces the spin coherence unless the temperature is decreased to the point where the thermal energy is reduced far below the magnitude of the spin-orbit coupling, $k_B T \ll \lambda$. For this reason, most studies of SiV^- are therefore performed in dilution refrigerators with temperatures below 100 mK, such that thermal phonons of energy equal to the SiV^- spin-orbit coupling, $\lambda \approx 50$ GHz are frozen out. These challenging experimental conditions led to a further search for new color centers that would alleviate these problems.

Substituting the silicon dopant for a heavier group IV element results in stronger spin orbit coupling [92], meaning that other group IV-vacancies can be operated at higher temperatures. This property led to the study of the GeV^- [50] and SnV^- [51, 94] color centers. The SnV^- in particular has been shown to operate at moderate temperatures approaching 2 K [26], where a dilution refrigerator is no longer required.

1.3 Nuclear Spin Quantum Registers

Most quantum protocols involving spin-photon interfaces require quantum information to be stored in an ancillary memory while the electron's memory is used for repeated entanglement attempts [21, 77]. The most common choice for this memory is a proximal host nuclear spin, such as the ^{13}C naturally present in the host diamond lattice [69, 77, 1, 17]. The use of plentiful host lattice nuclei even allows for large registers of up to tens of nuclear spins [18]. Other forms of host spin memories have also been demonstrated in silicon carbide [16], with rare-earths dopants yttrium orthovanadate [83], and with dark electron spins from proximal nitrogen substitutional P1 centers in diamond [27].

While these host spin memories form useful demonstrations of the ancillary quantum register concept, they have an important limitation. Namely, due to the random distribution of the spin in the host material, the strength of the coupling between the color center and the ancillary spin register is also random. Some fraction of color centers will have no suitable ancillary quantum register, decreasing yield. Further-

more, there is a direct trade-off between the yield of color centers with sufficiently strong coupling to a register, and the strength of the noise due to the spin bath, which decreases spin coherence. Even if a color center with good coupling to a register is found, then the control sequence to transfer information to the register must also be carefully calibrated to the random coupling strength of that particular color center. These difficulties can be solved by turning to a spin register of a nucleus that is intrinsic to the color center, such as the nuclear spin of one of the dopants that forms the color center. This has been demonstrated with an ^{14}N dopant in the NV^- [74, 18], and more recently with the ^{29}Si dopant in SiV^- [85].

While each group IV dopant has at least one isotope with nuclear spin $I > 1/2$, only the ^{29}Si has been investigated as a quantum register, with a coupling strength to the electron spin of approximately 70 MHz [82, 76]. The use of intrinsic nuclear spins in other group IV-vacancies remains understudied, with even the basic hyperfine coupling parameters only sparsely reported in the literature [26, 2], and therefore not conclusively assigned. This thesis will develop a detailed model of this coupling, and report clear signatures of the hyperfine coupling for the group IV-vacancies, resolving this open question in the field.

Chapter 2

Theory of Group IV Color Centers

2.1 Electron Orbitals

As discussed in section 1.2, the group IV-negative color centers in diamond consist of a single group IV atom (Si, Ge, or Sn) replacing a carbon atom in the diamond lattice, and located next to a carbon vacancy. The dopant occupies a split-vacancy position, meaning that it sits at the midpoint between the lattice positions of the two missing carbon atoms, giving it a D_{3d} symmetry (see Figure 2-1a). By convention, we will define the D_{3d} symmetry axis as being along the z direction, and the x direction lying perpendicular the axis of symmetry in one of the planes containing a nearest-neighbor carbon, as shown in Figure 2-1a.

The defect center disrupts the regular potential of the diamond lattice, creating localized orbitals that charge carriers from the diamond can occupy. These defect orbitals are understood to be primarily composed of the dangling sp^3 bonds originating from the carbons nearest to the two empty lattice sites in the defect, with some additional contribution from the group IV dopant orbitals and valence/conduction bulk-like states [35]. The D_{3d} symmetry of the defect limits how these various atomic orbitals can mix together to form defect states, as any orbital state of the defect must respect the symmetry of the defect. Each combination of atomic orbitals that form the defect states can therefore be systematically attributed to an irreducible representation of the D_{3d} symmetry group using group theory [93]. This group theory-based

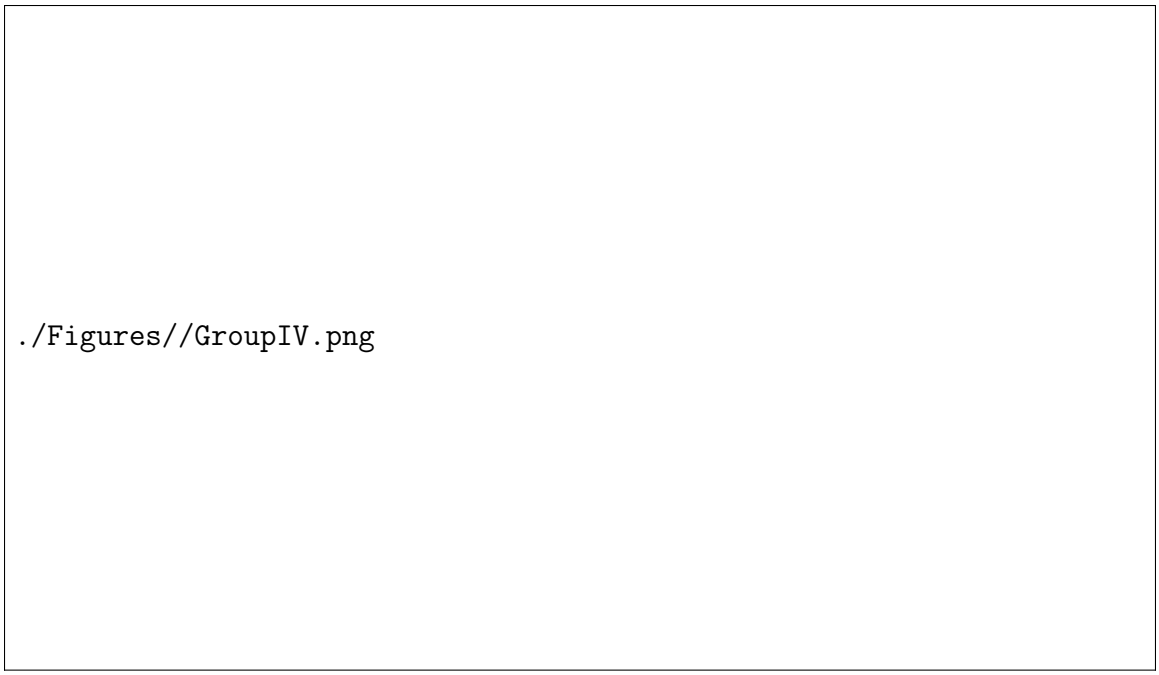

Figure 2-1: (a) Positions of the atoms in the group IV-negative color center. (b) Defect states relative to the band gap as predicted by DFT. (c) Electron density corresponding to each defect state

orbital attribution will be used throughout this thesis, and is outlined elsewhere in the literature for both the group-IV negatives [35, 42], as well as other color centers like the nitrogen-vacancy color centers [29]. For the group IV-negatives, it predicts that the six dangling bonds should produce defect orbitals that transform like the irreducible representations A_{1g}, A_{2u}, E_u, E_g under the symmetry operations of the D_{3d} symmetry group. The E_u and E_g representations are degenerate, and each therefore has a set of two linearly independent orbitals with the same energy, labeled $e_{ux/y}$ and $e_{gx/y}$ respectively, see Figure 2-1c.

More detailed studies using density functional theory (DFT) provide further details on the nature of the relevant defect orbitals. In particular, Thiering et al. [92] have done detailed DFT studies of the group IV-vacancy defects with excellent agreement with experimentally measured values. They find that in the negative charge state two e_g orbitals lie within the diamond band gap, and the e_u orbitals lie at the valence band edge. The orbitals corresponding to the other representations are energetically far from the band gap, and therefore do not contribute to the dynamics of

the color center. In the negative charge state, the e_u and e_g orbitals are completely filled with electrons, except for one hole which resides in one of the e_g orbitals in the ground state, see Figure 2-1b. The optical and ground state dynamics of the group IV-negative color centers can be understood almost entirely as the dynamics of the hole within these e_g and e_u orbitals. For example, the optically addressable transitions are due to promotion of the hole from the e_g to the e_u orbitals.

2.2 Ground State Perturbation Hamiltonian

This thesis will focus on the dynamics of the hole in the ground state, i.e. within the e_g orbitals. Within this ground state manifold, the hole has two degrees of freedom: (a) the orbital degree of freedom, where the hole moves between the two near-degenerate e_g orbitals, and (b) the spin degree of freedom, where the hole changes spin states. We can model the ground state manifold as a tensor product of these two degrees of freedom, resulting in four-level system basis composed of states

$$|\psi_i\rangle = \left|e_{gx/y}\right\rangle \otimes |\uparrow / \downarrow\rangle \tag{2.1}$$

From the naive group theory based arguments outlined in the previous section, we would expect the energy levels of these four states to be completely degenerate. In reality however, perturbations both intrinsic to the defect and from external sources will break the degeneracy. As shown diagrammatically in Figure 2-2, the total Hamiltonian for the electron spin system, $\hat{H}_S$, will be a sum of contributions from spin-orbit coupling, $\hat{H}_{SOC}$, strain $\hat{H}_{E_{gx/y}}$, and magnetic field $\hat{H}_B$.

$$\hat{H}_S = \hat{H}_{SOC} + \hat{H}_{E_{gx}} + \hat{H}_{E_{gy}} + \hat{H}_B \tag{2.2}$$

The forms of the four-level Hamiltonians for these perturbations can also be inferred from group theory [93, 29, 42], generally up to a constant factor that must be calculated from first-principles (e.g. using DFT) or measured experimentally. The results for the important perturbations on the group IV-negative color centers are summa-

rized below, taken from [42] unless otherwise stated.

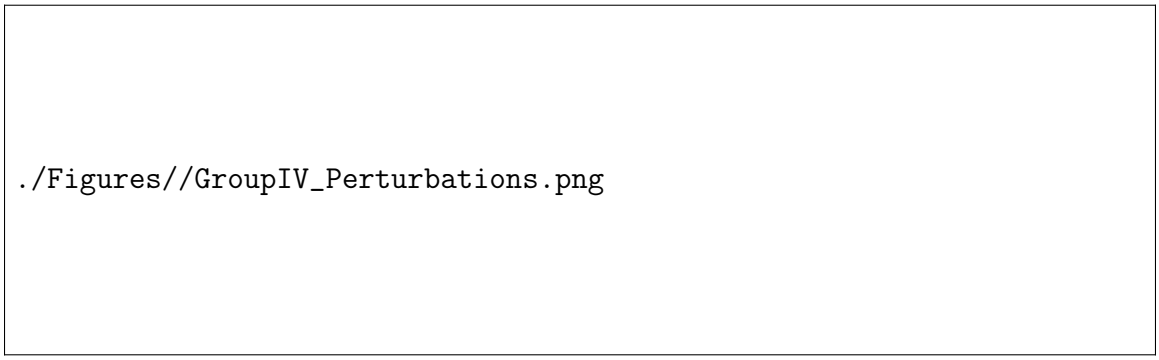

Figure 2-2: Perturbations on the ground state manifold

2.2.1 Spin-Orbit Coupling

Spin-orbit coupling is a coupling between the spin degree of freedom and the magnetic field caused by the orbital motion of the hole around the defect. Instead of representing the orbital degree of freedom in the e_{gx}/e_{gy} basis, it is convenient to use the basis $|e_{g\pm}\rangle = \frac{1}{\sqrt{2}}(|e_{gx}\rangle \pm i\,|e_{gy}\rangle)$. In this basis, using $\sigma_{x/y/z}$ to represent the Pauli spin matrices, the spin-orbit Hamiltonian can be written

$$\hat{H}_{SOC} = \frac{\lambda}{2}\sigma_z \otimes \sigma_z \tag{2.3}$$

The spin-orbit coupling causes a large splitting of the four e_g ground state manifold, into two, twofold degenerate branches, even in the absence of external perturbations. One branch will consist of states where the electron and orbital degrees of freedom are aligned ($|e_{g+}\uparrow\rangle$ / $|e_{g-}\downarrow\rangle$), while the other will have the two degrees of freedom anti-aligned ($|e_{g+}\downarrow\rangle$ / $|e_{g-}\uparrow\rangle$), with the ordering depending on the sign of λ.

2.2.2 Strain

Strain (stretching or compressing the diamond lattice) can be thought of as affecting the positions of the atoms around the group IV-negative color center. Since atomic positions determine the orbital energies, we expect that strain will produce some

perturbing Hamiltonian term on the ground state that will affect the orbital levels, but not directly affect the spin degree of freedom. While strain can be described as a rank two symmetric tensor with six independent components, the D_{3d} symmetry of the defect dictates that strain can only produce three inequivalent types of perturbations on the defect, transforming as the irreducible representations A_{1g}, and $E_{gx/y}$.

The A_{1g} term corresponds to strain that does not break the defect's symmetry, for example compression along the axis of symmetry. Though it may affect energy differences between orbitals of different symmetries, it will only result in a global shift of the e_g orbitals. We can therefore safely ignore A_{1g} strain for the purpose of calculating ground state properties, as it will not cause any mixing or shifting of the ground state orbitals relative to each other.

The E_g terms do break the defect's D_{3d} symmetry, and therefore can cause mixing that affects the ground state dynamics. E_g strain can be represented as a pair of perturbing Hamiltonian terms in the $|e_{g\pm}\rangle\,|\uparrow / \downarrow\rangle$ basis

$$\begin{aligned} \hat{H}_{E_{gx}} &= -\alpha\sigma_x \otimes \mathbb{1} \\ \hat{H}_{E_{gy}} &= -\beta\sigma_y \otimes \mathbb{1} \end{aligned} \tag{2.4}$$

where α & β can be further related to the strain applied to the diamond through the strain susceptibilities d & f[61]

$$\begin{aligned} \alpha &= d(\epsilon_{xx} - \epsilon_{yy}) + f\epsilon_{zx} \\ \beta &= -2d\epsilon_{xy} + f\epsilon_{yz} \end{aligned} \tag{2.5}$$

where the coordinate system is taken to be the standard coordinate system shown in Figure 2-1. The effect of E_g strain is therefore to cause a mixing mixing between the $|e_{g\pm}\rangle$ states, causing a splitting of the ground state manifold into two branches containing two degenerate levels, similar to spin-orbit coupling.

2.2.3 Magnetic Field

Applying a magnetic field to the defect breaks time-reversal symmetry, and is therefore expected to affect the spin degree of freedom. Magnetic field causes a Zeeman splitting

$$\hat{H}_B = \gamma_S \boldsymbol{B} \cdot \hat{\boldsymbol{S}} = \frac{1}{2}\gamma_S \left(B_x \mathbb{1} \otimes \sigma_x + B_y \mathbb{1} \otimes \sigma_y + B_z \mathbb{1} \otimes \sigma_z\right) \tag{2.6}$$

In principle γ_S need not be isotropic, and may have different values along the x/y versus the z directions. However, in practice this difference is found to be small, and we will use the free space value of $g\mu_B$, where g is the electron g-factor, and μ_B is the Bohr magneton.

In addition to the spin degree of freedom, the orbital degree of freedom may have some response to the magnetic field. This results in the orbital magnetic term

$$\hat{H}_{B_L} = q\mu_B B_z \sigma_z \otimes \mathbb{1} \tag{2.7}$$

Unlike the spin degree of freedom, the orbital degree of freedom is clearly only affected by the a magnetic field along the z axis. This behavior can be intuitively understood by noting that the $|e_{g\pm}\rangle$ states loosely correspond to a the $m_L = \pm 1$ states of the hole orbiting the defect with orbital angular momentum $L = 1$. The $m_L = 0$ state from group theory would correspond to the a_{1g} state, which as discussed in the previous section 2.1, are energetically far away from the e_g states. As the magnetic field along the x & y directions can only affect the levels through mixing of the $m_L = 0$ and $m_L = \pm 1$ states, the large energy difference between these states means that the contribution of the $B_{x/y}$ fields must be perturbatively suppressed. The magnetic field along z on the other hand will only cause a shifting of the $m_L = \pm 1$ states, and therefore must be included. The factor q is included to account for any differences between the free-space and solid-state susceptibility, such as that which is caused by the Jahn-Teller effect discussed below.

The net effect of the magnetic field is to cause a splitting of the spin sub-levels. When combined with the orbital splitting induced by spin-orbit coupling and strain

discussed in the previous two sections, this breaks the degeneracy within the two branches of the ground state manifold, resulting in four different energy levels.

2.2.4 Jahn-Teller Interaction

Group theory predicts that when the symmetry of a system allows for orbitals with degenerate energy levels, then there exists a distortion which will break the degeneracy of the system, raising the energy of one orbital and lowering the energy of the other. As discovered by Jahn and Teller [52], if the occupation of these orbitals is uneven, this necessarily implies that the system becomes unstable under these types of distortions.

As the e_g ground state orbitals of the group IV-color centers are degenerate and unevenly occupied, the Jahn-Teller effect should be included in any description of the ground state. In the specific case of the D_{3d} symmetry for the group IV-negatives, the distortion can be categorized as an $E_g \otimes e_g$ dynamic Jahn-Teller distortion [92] to a C_{2h}-symmetric configuration. The strong electron-phonon coupling that occurs during the Jahn-Teller distortion means that a complete description of the distortion would require solving the joint electron-phonon Hamiltonian. In this case, energy eigenstates can then no longer be described as separate electronic and vibrational states, but must be described as joint vibronic states. As the Jahn-Teller distortion is small for the group-IV negatives, instead of dealing with a complete description of the vibrational modes, we will follow the approximation outlined in [42], and instead assume that the effect of the Jahn-Teller distortion is to effectively quench certain defect parameters. In particular, the spin-orbit coupling parameter λ, and orbital magnetic parameter q will be smaller than otherwise expected.

2.2.5 Summary of Known Parameters

Parameters that are known experimentally or from DFT are summarized in table 2.1 below, with the values drawn from from [a][92], [b][38], [c][43], [d][61], [e][31], [f][60], [g][51], [h][94] [i][100].

Table 2.1: Summary of the ground state spin-orbit coupling parameter, orbital magnetic parameters, strain susceptibility of group IV-negatives reported from experiment and DFT calculations.

Defect	λ (GHz, DFT)[a]	λ (GHz, DFT quenched)[a]	λ (GHz, exp.)	q (exp.)	d (PHz, exp.)	f (PHz, exp.)
SiV^-	198	61	50[b]	0.1[c]	1.3[d]	-1.7[d]
GeV^-	532	207	181[e]	–	2.2[e]	–
SnV^-	2001	945	850[g]	0.15[h]	–	–
PbV^-	8360	4385	3900[i]	–	–	–

Chapter 3

Nuclear Hyperfine Interactions

3.1 Theory of Hyperfine Interactions

Much like electrons, nuclei may have a spin angular momentum with an associated spin operator and nuclear g-factor. The model Hamiltonian discussed in chapter 2 must then be modified to add the nuclear spin. We use the basis $|e_{g\pm}\rangle \otimes |\uparrow / \downarrow\rangle \otimes |m_I\rangle$, where m_I is the component of the nuclear spin aligned to the z direction. In the case of spin-1/2 nuclei, which corresponds to most of the nuclei of interest for the group IVs, $m_I = \pm 1/2$, and the basis can be written as $|e_{g\pm}\rangle \otimes |\uparrow / \downarrow\rangle \otimes |\Uparrow / \Downarrow\rangle$. All the Hamiltonian terms from chapter 2 do not affect the nuclear spin, and therefore we can simply take the tensor product with the identity acting on the nuclear spin states. The augmented Hamiltonian must include terms relating to the nucleus, namely the nuclear spin Hamiltonian, and the hyperfine interaction between the electron and nucleus. The total Hamiltonian will therefore be

$$\hat{H} = \hat{H}_S + \hat{H}_I + \hat{H}_{HF} \tag{3.1}$$

where $\hat{H}_S$ is the equation 2.2. The nuclear spin will interact with a magnetic field according to

$$\hat{H}_I = g_I \mu_N \boldsymbol{B} \cdot \hat{\boldsymbol{I}} = g_I \mu_N \left(\mathbb{1} \otimes \mathbb{1} \otimes B_x \hat{I}_x + \mathbb{1} \otimes \mathbb{1} \otimes B_y \hat{I}_y + \mathbb{1} \otimes \mathbb{1} \otimes B_z \hat{I}_z \right) \tag{3.2}$$

where g_I is the nuclear g-factor, $\mu_N = \frac{e\hbar}{2m_p}$ is the nuclear magneton, and $\left\{\hat{I}_x, \hat{I}_y, \hat{I}_z\right\}$ are the generalized spin operators associated with the nuclear total spin number I.

In the context of group IV-negatives, nuclear spins can take the form of neighboring ^{13}C nuclei in the diamond lattice, or the group IV dopant nucleus of an isotope that has non-zero spin. A list of nuclear isotopes that have spin and can be present in group IV-negatives, along with their spin properties and relative abundance are shown in table 3.1 with values taken from [80]. ^{13}C may exhibit hyperfine interactions with any of the group IV-negatives as it may be incorporated in a neighboring carbon site in the host diamond lattice, whereas the isotopes of other group IV elements may only have hyperfine interactions if they are the dopant atom in the associated group IV-negative defect.

Table 3.1: Stable nuclear isotopes that may exhibit hyperfine interactions with group IV-negatives. [80]

Isotope	Spin, I	g-factor	Quadrupole Moment (fm^2)	Relative Abundance (%)
^{13}C	1/2	+1.4048	0	1.07
^{29}Si	1/2	-1.11058	0	4.685
^{73}Ge	9/2	-0.19544	-17.0	7.76
^{115}Sn	1/2	-1.83766	0	0.34
^{117}Sn	1/2	-2.00208	0	7.68
^{119}Sn	1/2	-2.09456	0	8.59

The hyperfine interaction of interest in this thesis is an interaction between the unpaired electron and the dopant nuclear spin. The effect of the hyperfine interaction can be written in its most general form as

$$\hat{H}_{HF} = \hat{\boldsymbol{S}} \cdot \boldsymbol{A} \cdot \hat{\boldsymbol{I}} + \hat{H}_{IOC} + \hat{H}_Q \tag{3.3}$$

where $\boldsymbol{A}$ is the spin-spin hyperfine tensor, $\hat{H}_{IOC}$ is the nuclear spin-orbit coupling, and $\hat{H}_Q$ is the nuclear quadrupole moment.

In order to determine the hyperfine parameters, we need to understand the source of the electron-nuclear spin interaction. We can think of the hyperfine interaction as

resulting from the precession of the nuclear spin in the presence of the electric and magnetic fields caused by the unpaired hole spin. The unpaired hole can affect the nuclear spin in three ways, discussed in the following sections: (1) the dipole-dipole interaction with the nuclear spin, (2) the magnetic field due to the orbital motion of the hole, and (3) the electric field due the hole's charge via the nuclear quadrupole moment.

3.1.1 Dipole-Dipole Interactions

The dipole-dipole interaction results from the magnetic dipole field extending from the electron spin to the nucleus [8]. We can treat the nucleus as stationary (within the Born-Oppenheimer approximation), and average the dipole-dipole interaction over the hole spin distribution $\rho_S(\boldsymbol{r}) = \rho_\uparrow(\boldsymbol{r}) - \rho_\downarrow(\boldsymbol{r})$. The dipole-dipole interaction will then cause the $\boldsymbol{A}$ term in equation 3.3 as the result of two different terms. The first is an anisotropic term from the classical dipole-dipole interaction averaged over the electron spin density:

$$\boldsymbol{A}_{DD} = \frac{\mu_0}{4\pi} g\mu_B g_I \mu_N \int d\boldsymbol{r} \rho_S(\boldsymbol{r}) \frac{3\boldsymbol{r}\boldsymbol{r} - \boldsymbol{I}}{r^3} \tag{3.4}$$

where $\boldsymbol{I}$ is the 3x3 identity, and $\boldsymbol{r}$ is the distance from the nucleus. The D_{3d} symmetry of the group IVs force the dipole-dipole contribution of the hyperfine interaction with the dopant nucleus to be $A_{DD} \equiv A^{\parallel}_{DD} = -2A^{\perp}_{DD}$ [65].

The Fermi contact interaction is an additional hyperfine term that arises from the direct contact of the unpaired hole with the nucleus [8]. Unlike the dipole-dipole interaction, it is completely isotropic, depending only on the electron spin density at the nucleus, $\rho_S(0)$

$$\boldsymbol{A}_{FC} = A_{FC}\boldsymbol{I} = \frac{2\mu_0}{3} g\mu_B g_I \mu_N \rho_S(0)\boldsymbol{I} \tag{3.5}$$

The total dipole-dipole tensor $\boldsymbol{A}$ can then be expressed as the sum of the two terms

$$\boldsymbol{A} = \boldsymbol{A}_{DD} + \boldsymbol{A}_{FC} \tag{3.6}$$

3.1.2 Nuclear Spin-Orbit Interaction

The nuclear spin-orbit coupling (IOC) term, $\hat{H}_{IOC}$, arises from the interaction of the nuclear spin with the magnetic field caused by the orbital motion of the hole around the defect center. It can be expressed as

$$\hat{H}_{IOC} = -\frac{\mu_0}{4\pi}\frac{2g_I\mu_B\mu_N}{\hbar^2}\frac{\hat{\mathbf{L}}\cdot\hat{\mathbf{I}}}{r^3} \tag{3.7}$$

By analogy with the electronic spin-orbit coupling term, which is of the form $\hat{H}_{SOC} = -\lambda/2\hat{\mathbf{L}}\cdot\hat{\mathbf{S}}$ [42, 43], we can infer that in the basis defined in section 3.1, this will reduce to

$$\hat{H}_{IOC} = \frac{1}{2}\upsilon\sigma_z \otimes \mathbb{1} \otimes \hat{I}_z \tag{3.8}$$

where υ is a parameter quantifying the strength of the nuclear spin-orbit interaction. This results in an energy shift of the hyperfine levels of magnitude υ.

First-principles calculations can be employed to find the numerical value of this parameter, however we expect it to be negligibly small for two reasons. Firstly, the r^{-3} component of equation 3.7 will greatly suppress the strength of the IOC interaction to be at most roughly as strong as the dipole-dipole interaction ($< 5\%$ of the total hyperfine interaction as discussed later). Secondly, the orbital magnetic term in equation 2.7, $\hat{H}_{B_L} = q\mu_B\hat{\mathbf{L}}\cdot\mathbf{B}$, is known to have a small effective response $q \approx 0.1$. This can be attributed to a decreased effective orbital angular momentum due to the presence of the lattice. We would expect this effect to further decrease the IOC, making this term roughly 3 orders of magnitude smaller than the total hyperfine interaction discussed in the paper.

3.1.3 Quadrupole Interaction

The quadrupole interaction term $\hat{H}_Q$ arises from the non-spherical charge distribution of nuclear spins with $I > 1/2$, and is zero for $I \leq 1/2$, and it is therefore only applicable to the spin-9/2 isotope ^{73}Ge discussed in this thesis. The quadrupole moment of the nucleus can be thought of as two dipoles with opposite orientations to each other,

and displaced by a small amount from each other in the direction perpendicular to their axes. Intuitively, the opposing dipoles want to orient themselves in opposite directions along any applied electric field, and therefore the total torque applied to the system under a uniform electric field cancels out. If, however, the electric-field is non-uniform, then one of the dipoles may experience a slightly stronger electric field, and the whole system will therefore tend to align itself in a way depending on the electric field gradient.

The quadrupole interaction term therefore results in a energy shift dependent on the alignment of the nucleus with the gradient of the electric field, and takes the form

$$\hat{H}_Q = \hat{\mathbf{I}} \cdot \mathbf{Q} \cdot \hat{\mathbf{I}} \tag{3.9}$$

where $\mathbf{Q}$ is a matrix proportional to the electric potential's curvature at the nucleus, and the nuclear quadrupolar moment. If no external field is applied, the electric field curvature can only come from the electronic distribution around the defect. Similar to the hyperfine interaction matrix $\mathbf{A}_{DD}$, the defect's D_{3d} symmetry restricts the matrix $\mathbf{Q}$ to be diagonal, with $-2Q_\perp = Q_\parallel = Q$.

3.2 DFT Calculations of Hyperfine Parameters

3.2.1 Review of Density Functional Theory for Point Defects

Density functional theory (DFT) is a numerical method for calculating the properties of an interacting quantum many-body system without calculating the full many-body wavefunction. The central quantities in DFT, the ground-state energy and the density of the interacting particles, are in principle exact given the correct choice of functionals [46] (up to numerical approximations made during the calculation). In practice, however, the exact functional is not known and it is approximated using fictitious single-particle wavefunctions that interact with each other only via the density within the Kohn-Sham (KS) implementation of DFT [57]. While the KS single-particle orbital energies are not formally "real" quantities in the KS formalism of DFT, they

are often found to have very similar energies to the orbitals measured in experiment, and are therefore often interpreted as such.

DFT calculations have had tremendous success predicting material properties, including those of color centers. A single point defect in an infinite solid is approximated using a supercell, where the color center is embedded in a single unit cell of the host material, and then surrounded by a few pristine unit cells [33]. For sufficiently large numbers of pristine unit cells, the point defect is spatially separated from its periodic images, and its properties approach that of a single defect in an infinite host material.

State-of-the-art DFT calculations are able to relate the KS orbitals to the orbitals predicted from group theory in Section 2.1 [35], predict the thermodynamically stable charge state of the defect [97], the zero phonon line energy [92], the shape of the phonon sideband [3], and the magnitude of other perturbations on the color center such as spin-orbit coupling and Jahn-Teller distortion [92, 91]. These types of calculations have been extensively used to understand the properties of NV^- [90, 34], the negatively charged group IV-vacancies [92], the neutrally charged group IV-vacancies [91, 23], and to predict novel emitters [40] in diamond, as well as for color centers in other materials such as silicon carbide [14] and silicon [95]. We now apply this powerful tool to the prediction of hyperfine parameters.

3.2.2 Group IV Color Centers Hyperfine Parameters

In order to compute the dipole-dipole and Fermi contact contribution to the hyperfine parameters from first principles, we need to be able to evaluate both the distribution of electron spin density in the area immediately around the nucleus, as well as the exact spin density at the nucleus. If this spin density distribution is computed using pseudopotential KS-DFT, calculating the hyperfine parameters is complicated by the fact that the pseudopotential method is specifically designed to (a) smooth out the shape of the orbitals near the nucleus to reduce computational requirements, and (b) approximate the contribution of the core electrons as unaffected by the valence electron orbitals. While these approximations are good for typical DFT calculations, where calculated values do not depend on the details of the density near the nucleus,

they fall flat for hyperfine calculations that do require precise calculation of the spin distribution near the nucleus.

Point (a) can cause problems for evaluation of both the dipole-dipole and Fermi interaction where the valence spin density may be inaccurate near the nucleus. Point (b) also causes significant inaccuracy if, for example, the unpaired electron orbital does not have significant s-like character on the nucleus of interest. This means that the spin density will have a node near the nucleus, and equation 3.4 would therefore predict a low Fermi contact energy. However, polarization of the valence electrons can induce polarization of the core electrons, drastically changing the net spin density at the nucleus.

In this thesis, we use the QE-GIPAW package [36] within the Quantum Espresso DFT code [37]. This package uses the gauge-including projector augmented wave (GIPAW) [75] method to accurately reconstruct the valence electron orbitals near the nucleus, as well as core relaxation [8] to accurately find the spin density at the nucleus.

3.2.3 Dopant Nuclear Spin Ground State Hyperfine

For ground state calculations, we perform a spin polarized ionic relaxation calculation in Quantum Espresso with SiV^-, GeV^-, and SnV^- defect embedded in a 512 atom (4x4x4) cubic unit cell. The orbital fillings are specified so that the unpaired electron occupies the lowest energy orbital, and a D_{3d} symmetry is specified. We use the PBE functional [73] with an 80 Ry cut-off, and pseudopotentials generated using the atomic code with Quantum Espresso. After the ionic positions were relaxed, we then ran the GIPAW code using the g-factor values taken from table 3.1 to calculate the hyperfine parameters.

The resulting spin density isosurface plot for each calculation, as well as a cross-section of that spin density passing through the dopant nucleus is shown in Figure 3-1. The calculated hyperfine parameters associated with each nucleus are shown in table 3.2.

The ^{29}Si hyperfine can immediately be compared to the hyperfine values reported

Figure 3-1: (a-c) 3D plots of the spin density for Si, Ge, and Sn in the ground state (d-f) corresponding 2D cross-section of the spin density plots.

in the literature. Previous reports have used resonant spectroscopy to identify hyperfine splittings associated with ^{29}Si in the range of 66-70 MHz [82, 76, 85], in close agreement to the predicted hyperfine interaction. Of note is the fact that due to the small g-factor of ^{73}Ge, its hyperfine interaction strength appears to be deceptively small. Normalizing by their nuclear g-factors, Si, Ge, and Sn have, for example, normalised Fermi contact strengths of $A_{FC}^{Si,norm} = 57.81$ MHz, $A_{FC}^{Ge,norm} = 246.8$ MHz, and $A_{FC}^{Sn,norm} = 693.84$ MHz, respectively.

A trend of increasing hyperfine interaction strength moving towards the heavier dopants evident. Indeed, the hyperfine interaction of Ge and Sn, which do not have definitive attribution of hyperfine interaction strengths in the literature, are much larger than that of Si. This behavior is explained by examining the spin density plots 3-1. Whereas for SiV^- the spin density is almost exclusively from the dangling nearest-neighbor carbon bonds, the GeV^- and SnV^- defects have significant contribution from dopant atomic orbitals. As the spin density is higher near the nuclear spin this leads

Table 3.2: Dopant hyperfine interaction values

Isotope	Spin, I	A_{FC} (MHz)	A_{DD} (MHz)	Q (MHz)
^{29}Si	1/2	64.20	-2.34	0
^{73}Ge	9/2	48.23	-1.35	4.3
^{115}Sn	1/2	1275.04	-24.47	0
^{117}Sn	1/2	1389.09	-26.65	0
^{119}Sn	1/2	1453.27	-27.89	0

to a larger dipole-dipole and Fermi contact interaction, and correspondingly larger hyperfine interaction.

We also calculate the quadrupole interaction coefficient Q in the ground state for $^{73}GeV^{-}$, the only color center with a nuclear spin $I > 1/2$. We find that it is only 4 MHz, resulting in a largely negligible shift in energy levels compared to the larger Fermi contact term, and can therefore be safely ignored.

3.2.4 Dopant Nuclear Spin Excited State Hyperfine

The excited state calculations are performed in much the same way as the excited state calculations, except that the a ΔSCF DFT calculation is used to constrain the hole to the e_u excited state orbital. As we are only using a PBE functional, and not the HSE functional that is typically used for state of the art excited state calculations in diamond, the ΔSCF calculation is not expected to yield accurate excitation energies. However, the PBE functional can still give good orbital distributions, so we expect that it should lead to reasonably accurate hyperfine parameters. The resulting spin density plot for each excited state calculation, as well as a cross-section of that spin density passing through the dopant nucleus is shown in Figure 3-2. The calculated hyperfine parameters associated with each nucleus are shown in table 3.3.

The hyperfine interaction in the excited state is smaller than the ground state hyperfine interaction, which can be understood intuitively with a symmetry argument. In the ground state, the unpaired electron occupies an e_g, which is inversion symmetric, where as in the excited state it occupies an e_u, which is inversion antisym-

Figure 3-2: (a-c) 3D plots of the spin density for Si, Ge, and Sn in the excited state (d-f) corresponding 2D cross-section of the spin density plots.

metric. This means that there is a node in the unpaired electron orbital, and therefore less spin density at the inversion symmetry point, which is where the nuclear spin is located. We therefore expect only a smaller hyperfine interaction in the excited state.

3.3 Effects of Hyperfine Interaction on the Ground State

In absence of other perturbations, we can understand the effect of the hyperfine interaction described by equation 3.3 by breaking it into its $A_{\parallel} = A_{zz}$ and $A_{\perp} = A_{xx/yy}$ components. $A_{\parallel} = A_{FC} + A_{DD}$ can be simply understood as a shift of the energy levels depending on whether the electron and nuclear spin are aligned or anti-aligned. In the case of spin-1/2 nuclei, this simply splits the four electron-nuclear states into two doubly degenerate groups $|\uparrow\Uparrow\rangle$ / $|\downarrow\Downarrow\rangle$, and $|\uparrow\Downarrow\rangle$ / $|\downarrow\Uparrow\rangle$ split by $\frac{1}{2}A_{\parallel}$, as illustrated in the

Table 3.3: Dopant hyperfine interaction values

Isotope	Spin, I	A_{FC} (MHz)	A_{DD} (MHz)
^{29}Si	1/2	-30.68	32.57
^{73}Ge	9/2	5.03	14.30
^{115}Sn	1/2	386.74	230.43
^{117}Sn	1/2	421.34	251.05
^{119}Sn	1/2	440.80	262.65

first half of Figure 3-3a and c for ^{29}Si and ^{117}Sn respectively. In the case of the spin-9/2 ^{73}Ge, there are now five different degrees of alignment/anti-alignment. The 20-level system therefore breaks down into 10 degenerate pairs for states $|\uparrow, +m_I\rangle$ / $|\downarrow, -m_I\rangle$, where $m_I \in \left\{\pm\frac{1}{2}, \pm\frac{3}{2}, \pm\frac{5}{2}, \pm\frac{7}{2}, \pm\frac{9}{2}\right\}$. This is shown in the first half of Figure 3-3b.

The $A_\perp = A_{FC} - 2A_{DD}$ can be understood as a mixing of the non-aligned hyperfine levels. If only A_{FC} is present, then this will mix the aligned/anti-aligned levels resulting from $A_\parallel$ into states with well-defined total spin nuclear angular momentum $J = I \pm S$. The addition of the small anisotropic component A_{DD} splits the states further by the alignment of the angular momentum along z, m_j. For the spin 1/2 nuclei, the states are therefore split into a singlet $J = 0$ and triplet $J = 1$ state separated by A_{FC}. The $J = 1$ triplet is further split into a $m_j = 0$ singlet, and a $m_j = \pm 1$ doublet separated by by $\frac{3}{2}A_{DD}$. This effect is illustrated in the second half of Figure 3-3a-c.

In order to accurately model the hyperfine splitting that is observed in the group IV-negatives, we must take into account the other perturbations that can affect the spin system which were discussed in chapter 2.

3.3.1 Spin-Orbit Coupling

As discussed in previous sections, spin-orbit coupling splits the electron energy states according to whether they are aligned or anti-aligned with the orbital angular momentum. As the $A_\parallel$ contribution to the hyperfine splitting is a shift depending on how the nuclear spin is aligned with the electron spin, it is unaffected by spin-orbit

Figure 3-3: Hyperfine levels as a function of increasing $A_{\parallel}$ in the first half and $A_{\perp}$ in the second half (up to their ground state DFT values) for (a) ^{29}Si, (b) ^{73}Ge, (c) ^{117}Sn. Color indicates total spin orbital angular momentum $\langle J^2 \rangle$ from blue (electron and nuclear spin completely anti-aligned) to red (electron and nuclear spin completely aligned)

coupling.

Since the $A_{\perp}$ component of hyperfine mixes states with different electron spins, and cannot affect the orbital degree of freedom, it must mix states that have the same orbital angular momentum. However, states with the same angular momentum but opposite electron spins are split apart by the spin-orbit interaction, so the mixing must be perturbatively suppressed by a factor of λ. In the relevant limit for the group IV-negatives, where $\lambda \gg A_{\parallel}, A_{\perp}$, the spin orbit coupling splits the hyperfine levels into an upper and lower branch, where $A_{\perp}$ is effectively turned off. This is shown using the ground state DFT hyperfine values above in Figure 3-4.

Figure 3-4: Ground state energy levels as a function of increasing spin-orbit coupling λ for (a) ^{29}Si, (b) ^{73}Ge, (c) ^{117}Sn. Color indicates total spin orbital angular momentum $\langle J^2 \rangle$ from blue (electron and nuclear spin completely anti-aligned) to red (electron and nuclear spin completely aligned)

3.3.2 Strain

Strain mixes the orbital degree of freedom across the spin-orbit splitting. The $A_\perp$ term therefore stops being suppressed, as it can now mix terms within the same branch. In the limit of very large strain $\alpha, \beta \gg \lambda$, the states within the lower branch have the same orbital components, with the upper branch states all having an orbital component identical to each other and orthogonal to that in the lower branch. In this regime, the hyperfine splitting is identical to that without spin-orbit coupling. This is demonstrated in Figures 3-5,3-6, & 3-7 by adding E_{gx} strain α to a system with the DFT hyperfine values, and spin orbit values reported in table 2.1. These show only the lower branch energy levels as a function of increasing strain, subtracting out

the overall shift to the branch due to strain.

3.3.3 Magnetic Field

The addition of a magnetic field adds Zeeman splitting on top of the perturbations from the previous sections due to the electron (and the much smaller nuclear) gyromagnetic ratio. This is illustrated in figures 3-5,3-6, & 3-7.

Figure 3-5: Strain & Zeeman splitting of $^{29}SiV^-$ in the lower branch of the ground state. Upper plot shows splitting without B-field as a function of increasing strain α, with dashed lines indicating strains where B-field is simulated. Remaining plots show energy levels as a function of field applied, with the angle from the D_{3d} axis indicated to left of each row, and the strain indicated at the bottom of each column. Color indicates total spin orbital angular momentum $\langle J^2 \rangle$ from blue (electron and nuclear spin completely anti-aligned) to red (electron and nuclear spin completely aligned)

Figure 3-6: Strain & Zeeman splitting of $^{73}GeV^{-}$ in the lower branch of the ground state. Upper plot shows splitting without B-field as a function of increasing strain α, with dashed lines indicating strains where B-field is simulated. Remaining plots show energy levels as a function of field applied, with the angle from the D_{3d} axis indicated to left of each row, and the strain indicated at the bottom of each column. Color indicates total spin orbital angular momentum $\langle J^2 \rangle$ from blue (electron and nuclear spin completely anti-aligned) to red (electron and nuclear spin completely aligned)

Figure 3-7: Strain & Zeeman splitting of $^{117}SnV^-$ in the lower branch of the ground state. Upper plot shows splitting without B-field as a function of increasing strain α, with dashed lines indicating strains where B-field is simulated. Remaining plots show energy levels as a function of field applied, with the angle from the D_{3d} axis indicated to left of each row, and the strain indicated at the bottom of each column. Color indicates total spin orbital angular momentum $\langle J^2 \rangle$ from blue (electron and nuclear spin completely anti-aligned) to red (electron and nuclear spin completely aligned)

3.3.4 Effects of Jahn-Teller on Hyperfine Parameters

Intuitively, we expect the Jahn-Teller distortion that the group IV-negatives undergo to modify the shape of the orbitals, and therefore the spin density distribution around the nuclei. This in turn will modify the strength of the hyperfine coupling between the unpaired spin and the nuclei. As the Jahn-Teller effect distorts the D_{3d} symmetry of the defect into a lower C_{2h} symmetry, we expect to see breaking of the degeneracy of the A_{xx} and A_{yy} hyperfine parameters. In the case of zero strain, $A_{xx/yy}$ are perturbatively suppressed by the addition of spin-orbit coupling, and the symmetry

Config.	A_{FC} (MHz)	A_{DD}^{xx} (MHz)	A_{DD}^{yy} (MHz)	A_{DD}^{zz} (MHz)
D_{3d}	54.4	1.17	1.17	-2.34
C_{2h}	49.6	-0.456	-0.456	3.16

Table 3.4: Comparison of the hyperfine coupling for $^{29}SiV^-$ in the D_{3d} and C_{2h} configurations

breaking will only affect on the system through the shift in energy levels caused by the change in A_{zz} component. When we add additional strain back in to the system however, we re-introduce the $A_{xx/yy}$ parameters. In the limit of large strain, where the $A_{xx/yy}$ parameters are completely restored, in addition to shifts due to changing parameters, the $m_J = \pm 1$ states, which were previously degenerate, will be mixed into states $|\uparrow\Uparrow\rangle \pm |\downarrow\Downarrow\rangle$ separated by $\frac{1}{2}(A_{xx} - A_{yy})$.

The change in hyperfine parameters can be expressed as a shift in the hyperfine parameters. As the distortion may cause both an shift in the isotropic parameter, as well as break the degeneracy of $A_{xx/yy}$ parameters, we can model the effect of distortion using three parameters ΔA_{FC}, ΔA_{DD}, and $\Delta A_{\perp}$:

$$\begin{aligned} A_{xx} &\to A_{FC} + \Delta A_{FC} - 2(A_{DD} + \Delta A_{DD}) + \Delta A_{\perp} \\ A_{yy} &\to A_{FC} + \Delta A_{FC} - 2(A_{DD} + \Delta A_{DD}) - \Delta A_{\perp} \\ A_{zz} &\to A_{FC} + \Delta A_{FC} + A_{DD} + \Delta A_{DD} \end{aligned} \tag{3.10}$$

We estimate the size of these parameters by comparing the hyperfine parameters for SiV^- in the D_{3d} and C_{2h}configuration in a 3x3x3 cubic (216 atom) supercell, with the results shown in Table 3.4 For the 216 atom supercell, the results imply $\Delta A_{FC} = -4.8$ MHz, $\Delta A_{DD} = 5.5$ MHz, and $\Delta A_{\perp} < 0.01$ MHz. The distortion manifests mostly as a shift in the D_{3d} values, with the symmetry-breaking component $\Delta A_{\perp}$ remaining very small. Given these results, we estimate that Jahn-Teller distortion changes the magnitude of the hyperfine coupling by approximately 10% of the total value. Since Jahn-Teller does not qualitatively change the predictions, we leave a detailed study for future work.

3.4 Theoretical Hyperfine Spectra

When a spin-active isotope is present in a group IV color center, the ground and excited states both undergo hyperfine splitting. The single electron transition therefore splits into multiple transitions between the excited and ground states, with frequencies depending on the difference between the excited and ground states. The strength of the optical transitions is proportional to the matrix element $\langle\psi_{exc}|\hat{d}|\psi_{gnd}\rangle$, where $\hat{d}$ is the electric dipole operator. Since $\hat{d}$ only acts on the orbital degree of freedom [43], optical transitions cannot flip the nuclear or electronic spins, and only the spin-conserving transitions contribute significantly to the optical transition. We will here focus on the transition between the lower excited state spin-orbit branch and the lower ground state spin-orbit branch, commonly called the C-transition. However other transitions would exhibit similar behaviour.

As discussed in section 3.3, we are in the limit of large spin-orbit coupling, where the electro-nuclear ground state Hamiltonian in Eq. 3.1 produces a series of equally spaced hyperfine levels separated by $\frac{1}{2}A_{\parallel}^{gnd} = \frac{1}{2}(A_{FC}^{gnd} + A_{DD}^{gnd})$. Similarly, the excited state has hyperfine levels equally spaced by $\frac{1}{2}A_{\parallel}^{exc}$. The net result is that the single electron spin C-transition splits into multiple hyperfine transitions, separated by a spacing $A_{PLE} = \frac{1}{2}(A_{\parallel}^{exc} - \frac{1}{2}A_{\parallel}^{gnd})$. Strain further re-arranges the transitions into two groups associated with well defined angular momentum states.

Figures 3-8, 3-9, and 3-10a-c below show a visualization of this phenomenon for various strains. In the lower half of each subplot, we plot the ground state and excited state hyperfine energy levels as a set of lines rotated at $\pm 45°$ from the vertical, with color corresponding to the total angular momentum $\langle J^2\rangle$ of that state (red being $J = I + S$, and blue $J = I - S$). The intersection of each of the ground/excited state lines corresponds to a potential optical transition. A vertical line is plotted for each transition to the upper axis, with the intensity of the line corresponding to the predicted intensity of that transition. The lower plot is rotated and scaled in such a way that the position along the x-axis of the upper plot lines up with the transition frequency. A predicted spectrum, calculated as the intensity-weighted sum

of lifetime-limited Lorentzian for all the transitions, is shown in the upper half of the subplot. A 2D heatmap of the spectrum as a function of strain is shown in Figures 3-8, 3-9, and 3-10d.

Figure 3-8: (a-c) Predicted hyperfine spectra for $^{29}SiV^-$ at various strains, α. The bottom half of each plot shows the hyperfine levels in the ground/excited state. At each intersection a line whose intensity is proportional to the strength of the corresponding transition is plotted. The resulting predicted spectrum is shown in the upper half of the plot. Color indicates total spin orbital angular momentum $\langle J^2 \rangle$ from blue ($J = 0$) to red ($J = 1$) (d) Predicted spectrum as a function of strain.

For the spin-1/2 isotopes discussed in this paper, the hyperfine interaction causes four allowed transitions. Since the difference in hyperfine splitting is roughly the same order of magnitude as the lifetime-limited linewidth for SiV^- , these hyperfine transitions are never truly resolved as shown in Figure 3-8. In contrast, the hyperfine interaction of $SnV^-$is approximately 10 times larger than the expected 35 MHz lifetime-limited linewidth of the transition [94], making the hyperfine transitions directly resolvable, as shown in Figure 3-10. At zero strain, these occur in two

Figure 3-9: (a-c) Predicted hyperfine spectra for $^{73}GeV^{-}$ at various strains, α. The bottom half of each plot shows the hyperfine levels in the ground/excited state. At each intersection a line whose intensity is proportional to the strength of the corresponding transition is plotted. The resulting predicted spectrum is shown in the upper half of the plot. Color indicates total spin orbital angular momentum $\langle J^2 \rangle$ from blue ($J = 4$) to red ($J = 5$) (d) Predicted spectrum as a function of strain.

degenerate pairs separated by A_{PLE}: at lower frequency between the $m_J = \pm 1$ hyperfine states in the ground/excited level (C_{H1}), and between the two $m_J = 0$ states at a higher frequency (C_{H0}). The two peaks and their splitting A_{PLE} are labeled for $^{117}SnV^{-}$ in Fig. 3-10a. The $m_J = \pm 1$ states are unaffected by strain, while the $m_J = 0$ states mix and separate in both ground and excited manifolds. The strain-induced mixing splits the C_{H0} peak in the spectrum into two peaks, labeled C'_{H0} and C''_{H0}, each having half the intensity of the C_{H1} peak, with a splitting δ labeled in Fig. 3-10b.

Similarly for the spin-9/2 ^{73}Ge isotope, we expect 20 hyperfine transitions, in 10 degenerate pairs which are equally spaced by A_{PLE}. The hyperfine parameters predicted by DFT for $^{73}GeV^{-}$ are small because of ^{73}Ge's small gyromagnetic ratio

Figure 3-10: (a-c) Predicted hyperfine spectra for $^{117}SnV^-$ at various strains, α. The bottom half of each plot shows the hyperfine levels in the ground/excited state. At each intersection a line whose intensity is proportional to the strength of the corresponding transition is plotted. The resulting predicted spectrum is shown in the upper half of the plot. Color indicates total spin orbital angular momentum $\langle J^2 \rangle$ from blue ($J = 0$) to red ($J = 1$) (d) Predicted spectrum as a function of strain.

compared to the other group-IV elements, with the Fermi contact parameter predicted to be 48 MHz in the ground state. The resulting $A_{PLE} = -13.78$ MHz, smaller than the expected lifetime-limited linewidth for GeV^- of 26 MHz [12], and it is therefore not possible to optically resolve the hyperfine transitions. Nevertheless, the overlapping transitions result in a spectral line broadened by approximately $9|A_{PLE}| = 124$ MHz with a very non-Lorentzian flat-topped lineshape. Strain splits the flat-topped emission peak into two peaks corresponding to the transitions between the $J = 5$ levels at lower energy, and $J = 4$ levels at higher energy.

Chapter 4

Measurement of Hyperfine Signatures in Group IV Color Centers

4.1 Isotope-Selectively Implanted Diamond

In order to characterize the hyperfine parameters, we need a sample that allows for easy distinction of spin neutral and spin active isotopes in the group IV color centers. While different isotopes are chemically indistinguishable, they can be separated by mass spectroscopy due to their differing atomic mass. This capability is combined with spatially selective implantation through a focused ion-beam (FIB) at the Sandia National Laboratory to prepare samples where different spatial regions have been implanted with a selection of different spin neutral and spin active isotopes of group IV elements.

The samples were prepared from a single-crystal diamond plate ([N]$<$ 5 ppb) purchased from Element Six. We performed a 7 μm strain relief etch of the top diamond surface with Ar/Cl_2 and O_2 by reactive ion etch (RIE), and patterned alignment markers and QR codes [88] using electron beam lithography 180 nm with silicon nitride as a hard mask. A thin layer of gold ($\sim$ 50 nm in thickness) was then deposited and lifted off in HF acid, leaving metal covering only the alignment markers for optimal imaging contrast crucial for alignment during the subsequent ion implantation step. Shown in Figure 4-1a is a map of one of the samples prepared for this purpose,

Figure 4-1: (a) Diagram of the implanted isotopes in the diamond sample, with selected alignment marks shown in gray for scale. (b) Diagram of implant pattern within one of the regions, showing the arrangement of alignment marks, implant grid, and dose sweep. (c) Mass spectrogram for Sn isotopes. Peaks due to neighbor ing isotope masses overlap, indicating imperfect isotopes selection.

showing regions implanted with ^{28}Si, ^{29}Si, ^{74}Si, ^{74}Ge, ^{116}Sn, ^{117}Sn, ^{118}Sn, ^{119}Sn, ^{120}Sn, ^{120}Sn, and ^{124}Sn. Within each region, we implanted isotopically-purified group IV elements in a 1 μm pitch square grid, with an increasing dose of emitters, as shown in Figure 4-1b, with doses swept between 10 and 10^5, 10^6, 10^7, and 10^8 in different regions. Different regions were also implanted with different energies, targeting 25 nm and 75 nm depths based on SRIM calculations [103]. All measurements in this thesis were performed at the 75 nm depth implant, and in a region with approximately 100 ions per spot, corresponding to 1-5 emitters per spot given color center creation yields of approximately 1-5% [98]. Given the large inhomogeneous linewidth compared to the typical homogeneous linewidth, we expect fewer than 0.1% of emitters to have spectrally overlapping emission peaks. The implanted dopants were then converted to emitters by performing a high-pressure high-temperature (HPHT) anneal ($>$ 7 GPa

at 1950°C) by Element Six.

The separation of the implanted isotopes is not perfect, and especially for the tin isotopes, which have a small relative mass difference. A mass spectrogram is shown in Figure 4-1c, where the peaks corresponding to the labeled tin isotopes overlap.

4.2 Experimental Characterization of Color Centers

In order to measure the true hyperfine optical spectra predicted in Section 3.4, we need to measure the photoluminescent emission of the group IV color centers. This is done at cryogenic temperatures such that the optical transitions are not thermally broadened. We use a confocal setup, shown in Figure 4-2, which consists of a excitation path and collection path.

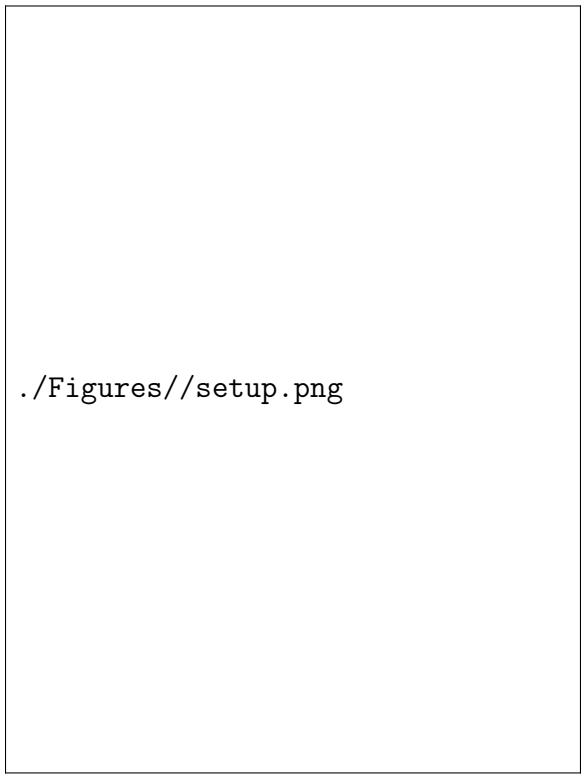

Figure 4-2: Confocal setup used for emitter measurements.

In the excitation path, laser light in the 600-620 nm range, provided by M^2 Solstis and EMM mixing modules, passes through an electro-optic modulator (EOM) for fast

tuning, then through a galvo system to direct it onto a desired spot in the microscope field of view. A 4f lens system is used to re-focus the laser laser light on to the back aperture of an objective, located in a Montana Cryo Systems Cryostat, which holds the sample at 5 K. The objective focuses the laser light onto a near diffraction limited spot on the sample which can be scanned to select the desired emitter. Fluorescence from the group IV color centers then passes back through the objective, 4f, and galvo, and is split off from the excitation path using a 90:10 beam-cube. The collection path is then fiber coupled to allow connection to a single-photon counting avalanche diode (SPAD), or an optical spectrometer. A flip mirror is also used to optionally send the light to an electron-multiplying CCD (EMCCD) camera for sensitive wide-field imaging.

4.2.1 Photoluminescence Excitation Spectroscopy

The narrow spectral hyperfine features that we wish to identify are below the resolution of most spectrometers. Rather than performing traditional photoluminescence (PL) spectroscopy, we perform photoluminescence excitation (PLE) spectroscopy to resolve these fine features. This involves sweeping the excitation wavelength across an optical transition, and measuring the intensity of the resulting fluorescence. When the excitation light is resonant with an allowed optical transition, the emitter will be excited at a much larger rate than with off-resonant excitation. Since the linewidth of the tunable laser used to excite the emitter can be much less than the optical transition's natural linewidth, PLE spectroscopy allows us to fully resolve the spectral fine structure. In order to isolate the laser light from the color center emission, we use the color center's phonon sideband (PSB). The emitter is coupled to vibrational modes in the lattice, and it therefore has some finite probability of emitting a photon and phonon at the same time when excited. Since the phonon carries some fraction of the energy, the photons that are emitted during this process will have a lower energy (longer wavelength), and can therefore be separated from the laser light by a longpass optical filter. We use a 620 nm longpass filter to isolate the 602 nm GeV^- PSB, and 635 nm longpass to isolate the 619 nm GeV^- PSB.

4.2.2 Wide-field Photoluminescence Excitation Spectroscopy

To conclusively identify hyperfine spectral signatures, it is necessary to collect spectra from large numbers of emitters. While this can be accomplished using traditional confocal PLE, this becomes a very time consuming process, as the slow excitation sweep must be performed at each emitter. We instead use wide-field PLE (WFPLE) [88], which allows for PLE measurements to be performed over a large number of emitters in a microscope field of view in one simultaneous excitation frequency sweep. To perform WFPLE, we added a lens mounted on a flip mirror into the excitation path which focuses the laser excitation onto the backplane of the objective. The laser light then illuminates a large portion of the objective's field of view rather than a diffraction limited spot. The fluorescence from all the emitters' PSBs illuminated by the laser is imaged onto the EMCCD camera, and recorded at each frequency step. For all WFPLE experiments, we use approximately 7 μW of resonant power and 35 μW of green power, as measured before the objective, and spread over an area of approximately 25 μm.

To convert the WFPLE data to PLE spectra, we selected the frequency and location of bright spots that corresponded to emitters. Since a diffraction limited spot is larger than a single pixel, to capture fluorescence on neighboring pixels, we perform a Gaussian-weighted average over a 7x7 pixel area around the spot of interest with a standard deviation of 2 pixels. The set of Gaussian-weighted averages for each frequency frame and location of interest then correspond to the PLE spectrum for each spot. A representative wide-field frame for ^{117}Sn at a single frequency, and the maximum over all frequencies is shown in Figure 4-3.

4.3 Experimental PLE Hyperfine Signatures

4.3.1 Photoluminescence of GeV$^-$

We start our search for hyperfine signatures by performing WFPLE on regions implanted with spin-9/2 ^{73}Ge and spin-9 ^{74}Ge. We show representative PLE spectra

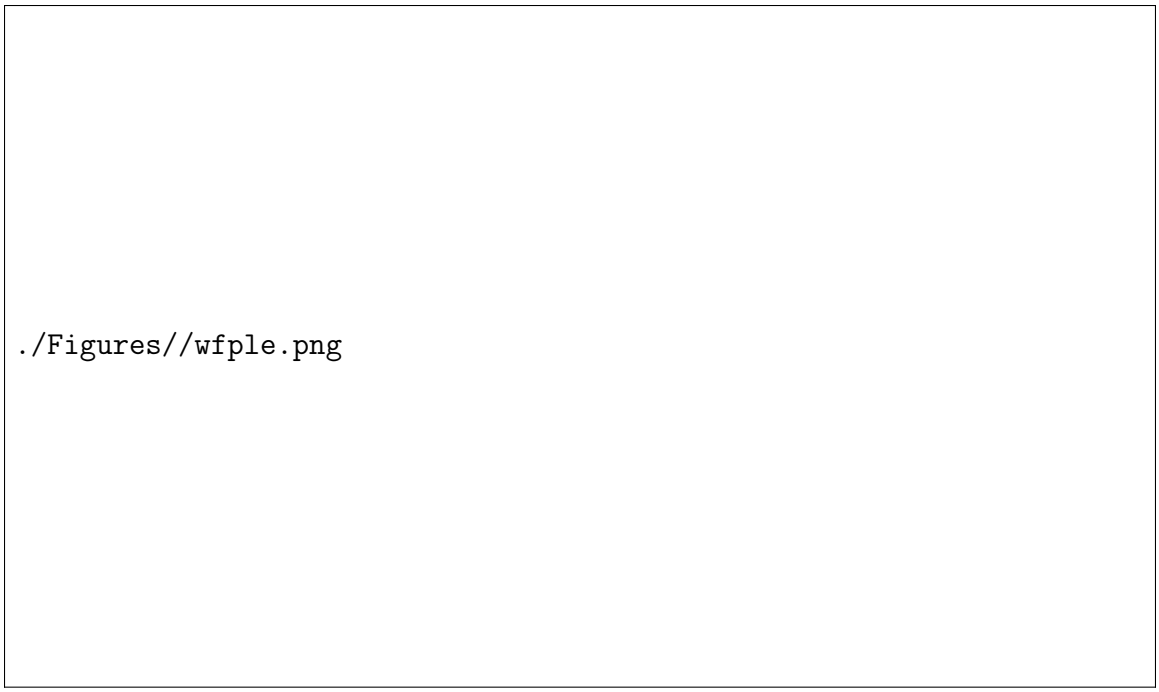

Figure 4-3: (a) Single frame of WFPLE data at a frequency of 484.172547 THz. (b) Maximum intensity across an entire 15 GHz PLE frequency sweep. Color is used as a visual aid to give an idea of the frequency at which maximum intensity occurs.

extracted from the WFPLE data in Figure 4-4a-b, along with a Lorentzian fit, where each frequency has been shifted so that they are relative to the fit's center frequency. As discussed in Section 3.4, we do not expect to be able to resolve each of the 10 transitions, but we do expect a broadening on the order of 100 MHz, and a non-Lorentzian lineshape. Indeed, we plot the averaged PLE spectra of 242 $^{73}GeV^{-}$ emitters and 195 $^{74}GeV^{-}$ emitters in Figure 4-4c, and see that the $^{73}GeV^{-}$ spectrum is substantially broader. In Figure 4-4d, we plot a histogram of the Lorentzian linewidth fits of the $^{73/74}GeV^{-}$ emitters. The average linewidth for $^{73}GeV^{-}$ is 262(7) MHz, roughly 70 MHz broader than the 190(5) MHz average linewidth for $^{74}GeV^{-}$ under the same laser power.

To confirm that this broadening is a result of hyperfine coupling, we performed confocal PLE at varying magnetic field, as shown in Figure 4-5. We fit this data using the hyperfine model of the isotope, fitting only a linewidth of 72(3) MHz, and $A_{PLE} = -12.5(5)$ MHz, which is within 10% of the DFT prediction. At zero field, the PLE spectrum with near-lifetime limited linewidth exhibits a flat-topped line shape

Figure 4-4: (a, b) Representative PLE data from WFPLE frames for $^{73/74}GeV^{-}$. (c) Comparison of the WFPLE data for $^{73/74}GeV^{-}$ averaged over all PLE spots relative to the fitted peak frequency. (d) Histogram of the Lorentzian linewidths from the fits for $^{73/74}GeV^{-}$.

due to the overlapping transitions, as discussed in Section 3.4. As the magnetic field is increased, the electro-nuclear levels separate into two groups of levels with the spins aligned/anti-aligned with the magnetic field. At intermediate field strengths (around 0.1 T), only the transitions from the two groups near zero detuning still overlap, and a characteristic central hump surrounded by two broad shoulders appears. The non-Lorentzian lineshape of the PLE transition further highlights that this lineshape comes from multiple overlapping hyperfine transitions.

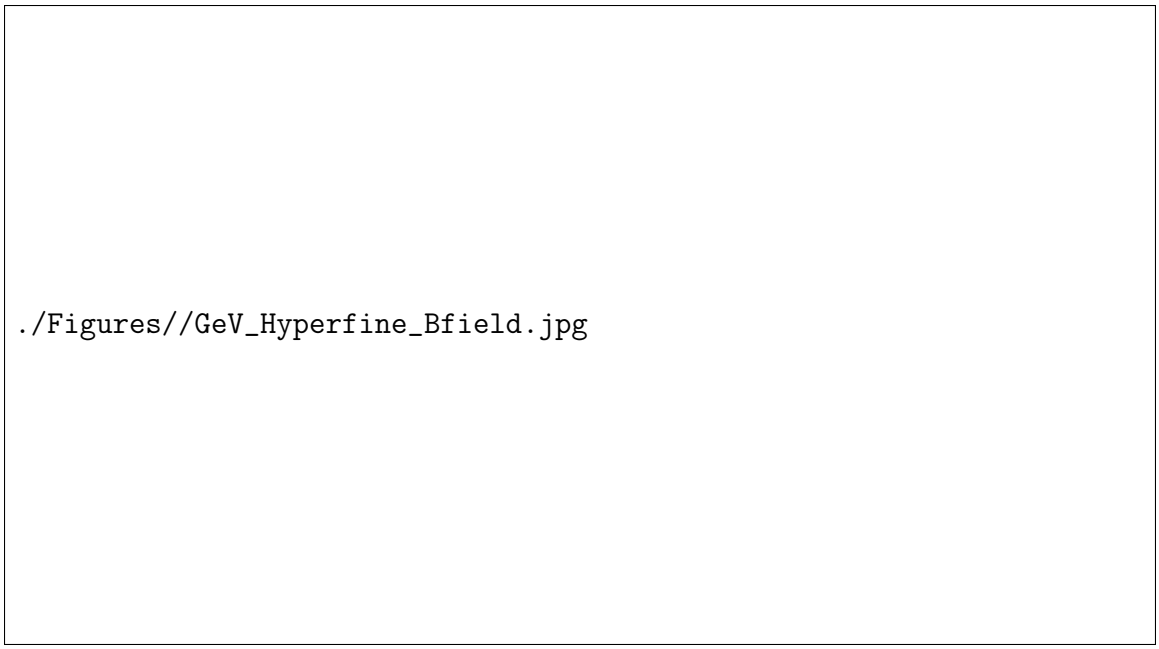

Figure 4-5: Plot of the confocal PLE intensity of a $^{73}GeV^{-}$ as a function of magnetic field. Red lines indicate fit to model.

4.3.2 Photoluminescence of SnV^{-}

For the spin active tin isotopes, we would expect to see two distinct hyperfine transitions due to the spin-1/2 nucleus directly observable in the PLE spectra, as discussed in Section 3.4. This can be seen in WFPLE spectra, averaged over around 100 sites for each of the isotopes $^{117}SnV^{-}$, $^{118}SnV^{-}$, $^{119}SnV^{-}$, and $^{120}SnV^{-}$ in Figure 4-6. It is clear that additional spectral features appear for the two spin-1/2 isotopes ^{117}Sn and ^{119}Sn that are not present for the spin-0 isotopes ^{118}Sn and ^{120}Sn.

To further characterize these hyperfine levels, we fit the PLE spectrum for each SnV^{-} individually with either a single Lorentzian peak (representing a spin-0 isotope), or three Lorentzian peaks with a 2:1:1 intensity ratio (corresponding the three transitions C_{H1}, C'_{H0}, and C''_{H0} for a spin-1/2 isotope). The fit is defined by two parameters: (1) the splitting between the C_{H1} and C_{H0} peaks determined by the hyperfine interaction strength, A_{PLE}, and (2) the strain-related splitting between the C'_{H0} and C''_{H0} peaks δ, as illustrated in Fig. 3-10a, b.

As summarized in Tab. 4.1, the 3-peak hyperfine feature is observed for more than 80% of the emitters in the two spin-1/2 isotope-implanted regions, whereas it

Figure 4-6: (a-d) Representative PLE data from WFPLE frames for $^{117\text{-}120}SnV^-$. Black lines indicate fit to model. (e) Comparison of the WFPLE data for $^{117\text{-}120}SnV^-$ averaged over all PLE spots relative to the fitted lowest frequency peak. (d) Histogram of the Lorentzian linewidths from the fits for $^{73/74}GeV^-$.

is present in less than 20% of the emitters in the spin-0 isotope-implanted regions. Performing a χ^2 test on the number of emitters with the multi-peak PLE spectra in the spin-0 vs spin-1/2 regions, we conclude with a high degree of certainty that the multi-peak PLE is associated with the spin-1/2 isotopes ($p < 10^{-5}$). The bulk of the emitters of the wrong type likely come from imperfect isotope separation during the implantation (see Figure 4-1). We can therefore conclusively assign the multi-peak feature to the spin-1/2 isotopes of tin. This result also clarifies a previous result showing an SnV^- hyperfine interaction strength of 40 MHz [26], an order of magnitude smaller than the ground state hyperfine coupling predicted in this paper. We now assess this report as the hyperfine coupling to a nearest-neighbor ^{13}C nucleus, since it is closer in magnitude to previous predictions for ^{13}C hyperfine coupling [58].

Table 4.1: Hyperfine statistics for the different SnV^- isotopes.

Isotope	Spin	Number of emitters.	Fraction w/Hyperfine Peaks (%)	A_{PLE} (S.E.) (MHz)
^{117}Sn	**1/2**	**136**	**87.5**	**445(9)**
^{118}Sn	0	119	16.0	–
^{119}Sn	**1/2**	**109**	**84.4**	**484(8)**
^{120}Sn	0	93	6.4	–

The distribution of hyperfine parameters A_{PLE} and δ for $^{117}SnV^-$ and $^{119}SnV^-$ are shown in Fig. 4-7, and the mean value is summarized for all isotopes in Tab. 4.1. We note that A_{PLE} is larger for ^{119}Sn than it is for ^{117}Sn. This is to be expected since the hyperfine coupling parameters are directly proportional to the nuclear gyromagnetic ratios [89] and indeed we find the ratio $A_{PLE,^{119}Sn}/A_{PLE,^{117}Sn} = 1.09(0.04)$ to be in good agreement with $g_{^{119}Sn}/g_{^{117}Sn} = 1.05$. The parameter δ distribution does not differ substantially between the two isotopes, as it depends only on the strain distribution that the two isotopes experience, which we do not expect to be vary.

Finally, we performed magneto-optic PLE by varying the magnitude of the B-field applied to a $^{117}SnV^-$, as shown in Figure 4-8a. We fit this data using the hyperfine model from Chapter 3, finding $A_{PLE} = -459(3)$ MHz, $\alpha = 55(3)$ GHz, and a power-broadened linewidth of 336(3) MHz. The simpler level structure compared to $^{73}GeV^-$ allows us to directly track the trajectory of the transitions as a function of field strength. The magnetic field breaks the degeneracy of the C_{H1} peak's two constituent transitions, producing two peaks labeled $C_{H1}^{\pm}$, corresponding to transitions between the ground and excited $m_J = \pm 1$ total angular momentum states. Due to the combined effect of an anti-crossing of the $m_J = 0$ ground states at zero magnetic field and the much weaker anti-crossing of the $m_J = 0$ excited states (see Figure 4-8b-c), the C_{H0} transitions exhibit an anti-crossing near zero-field. For a sufficiently strained emitter, the strong coupling maintains optical access to the hyperfine levels at this ground level anti-crossing point.

Figure 4-7: Bottom left pane is a scatter plot of the fitted hyperfine parameters A_{PLE} and δ. Corresponding histograms are shown to the left and above the scatter plot.

Figure 4-8: (a) Plot of the confocal PLE intensity of a $^{117}SnV^-$ as a function of magnetic field. Light red lines indicate fit to model, dark red lines show the fitted transitions frequencies for the transitions C'_{H0}, C''_{H0}, and $C^{\pm}_{H1}$. (b/c) Corresponding excited/ground state energy levels showing the anti-crossing between the $m_J = 0$ states in the ground level.

Chapter 5

Outlook

This thesis developed a complete model of the hyperfine interaction for the negatively charged group IV-vacancy color centers, and performed first-principles calculations to determine the hyperfine parameters. We predict a large increase in the hyperfine parameters moving down the group-IV column of the periodic table due to the increasing contribution of the dopant orbitals to the spin density. We further show that spin-orbit coupling and strain must both be accounted for when modeling the resulting hyperfine levels. We then experimentally measured optical hyperfine signatures of $^{73}GeV^{-}$, $^{117}SnV^{-}$, and $^{119}SnV^{-}$. In particular, the spin-active SnV^{-} color centers show a clearly resolvable optical multi-peak feature compared to the spin-neutral isotopes due to the large hyperfine coupling to the intrinsic tin nucleus.

We now compare the experimental and theoretical results, and briefly discuss the outlook for the use of the germanium and tin nuclear spins as quantum registers.

5.1 Summary of Predicted and Experimental Hyperfine Parameters

We show a summary of the hyperfine values predicted from DFT for the group IV color centers, as well as the hyperfine PLE parameters for the three spin-active isotopes we measured in Table 5.1. The predicted parameters are all within roughly 20% of the

measured experimental values, with the difference likely being due to a combination of a few errors in the DFT prediction. Firstly, the PBE functional used for the DFT calculations is known to be inferior to hybrid functionals such as HSE06 for the prediction of DFT properties. Secondly, the QE-GIPAW package does not symmetrise the PAW orbitals after recovering the true density. This results in substantial valence electron density near the nucleus in the excited E_u state, even though group theory dictates that there should not be none. While there may be some electron density due to electronic core relaxation in the excited, we expect that DFT value is an overestimate of this density. Finally, the Jahn-Teller distortion, briefly discussed in Section 3.3.4 but neglected throughout the rest of this thesis, will also shift the measured hyperfine parameters. Accounting for these factors in a more detailed DFT calculation should lead to more accurate hyperfine predictions.

Table 5.1: Summary of hyperfine parameters predicted by DFT and measured experimentally

Isotope	Spin	A_F^{gnd} (MHz)	A_{DD}^{gnd} (MHz)	A_{FC}^{exc} (MHz)	A_{DD}^{exc} (MHz)	A_{PLE} (MHz)	A_{PLE} (exp.,MHz)	DFT error (%)
^{29}Si	1/2	64.20	-2.34	-30.68	32.57	-29.98	–	–
^{73}Ge	9/2	48.23	-1.35	5.03	14.30	-13.78	-12.5(5)	9.2
^{115}Sn	1/2	1275.04	-24.47	386.74	230.43	-316.70	–	–
^{117}Sn	1/2	1389.09	-26.65	421.34	251.05	-345.02	-445(9)	22
^{119}Sn	1/2	1453.27	-27.89	440.80	262.65	-360.96	-484(8)	26

5.2 Outlook for GeV$^-$ Nuclear Spin Registers

The small gyromagnetic ratio of ^{73}Ge limits the strength of the hyperfine interaction such that the individual hyperfine transitions are not resolvable. The manipulation of the nuclear quantum register would therefore have to be performed via the electron spin. Compared to heralded entanglement, such local operation nuclear spin operations may nevertheless be of very high fidelity [18]. In the highly strained regime, the separation of the hyperfine transitions split into resolvable $J = 4/5$ groups, allowing the hyperfine levels to be partially initialized optically without the electron spin. This may simplify quantum register manipulation, further enhancing fidelity compared to

existing schemes.

The spin-9/2 in ^{73}Ge has a 10-level nuclear memory. In the large electronic spin-orbit coupling regime, the quadrupole coupling creates an anharmonic shift of Qm_J^2 of the eigenstates $|\uparrow / \downarrow\rangle |m_J\rangle$. If the nuclear spin sublevels are to be addressed individually, the anharmonicity sets the speed at which they can be manipulated, as a Rabi frequency exceeding the anharmonicity will cause unwanted driving of the wrong transition. The predicted $Q = 4.3$ MHz indicates that it should be possible to address the nuclear levels individually at MHz speeds. This presents the interesting possibility of having just over three qubits worth of quantum information stored within the intrinsic nuclear spin register, perhaps allowing for more sophisticated error correction to be performed using local operations [70]. The high fidelity local operations may improve quantum operation fidelity in a large network compared to other proposals with simple spin-1/2 registers [21]. The large quantum registers size also opens the possibility of the generation of large cluster photonic clusters states as resources for quantum protocols, using only spin-photon entanglement and local register operations [62].

The nuclear quadrupole moment also means that the nuclear spin can potentially be driven directly by an electric field [5]. This rather unique capability means that several GeV$^-$ could be operated independently by low-crosstalk electric field drives in dense arrays along a waveguide [99], further improving the ability to integrate these color centers.

5.3 Outlook for SnV$^-$ Nuclear Spin Registers

While the SnV$^-$ isotopes have a more conventional spin-1/2 intrinsic memory, the strong hyperfine coupling means that the hyperfine levels can be directly optically accessed. The direct optical access of the hyperfine levels also allows for the possibility of direct transfer of photon states to the nuclear memory without using the electron spin as an intermediary, which may enhance spin-photon entanglement fidelity compared to existing schemes [85]. Optical initialization and readout of the

nuclear spin via this hyperfine optical transition has been demonstrated in a separate work [72].

With non-zero strain applied to the defect at zero magnetic field, our model predicts a magnetic-field insensitive transition between the $|J = 0/1, m_J = 0\rangle$ ground states. Operating at this anti-crossing makes the levels magnetically insensitive to first order, suppressing the effect of magnetic noise [15, 56, 71]. Nuclear spin bath magnetic noise has been shown to have a large effect on the coherence of group-IV color centers in previous work [11, 69, 26], so operating in such a regime may improve coherence.

Finally, the strong coupling to the noisy electron spin raises the question of whether the nuclear spin coherence will be adversely affected. Due to nuclear spin-orbit coupling, a similar mechanism that limits the electron spins T_2 to roughly the orbital T_1 [53] may limit the nuclear T_2. Though further study is required to find the magnitude of the nuclear spin-orbit interaction, as outlined in Section 3.1.2 the coupling is expected to be small. In this case the nuclear spin coherence will not be limited by the orbital T_1, and likely only by the electron spin T_1, which is quite long even at elevated temperatures [94]. Since the hyperfine levels are optically resolvable at zero field, zero-field operation may allow the hyperfine level qubits to be initialized, manipulated, and measured at higher temperatures than what is currently practical for the electronic fine structure.

5.4 Conclusion

The presence of the strongly coupled memory in the well-established group-IV color center platform will allow future experiments to leverage their bright, high-quality optical emission in a new regime of quantum experiments. The clear identification of the hyperfine parameters of GeV^- and SnV^- therefore lays the groundwork for future work to use these nuclear spins as local memories for quantum information applications.

Bibliography

[1] M. H. Abobeih, Y. Wang, J. Randall, S. J.H. Loenen, C. E. Bradley, M. Markham, D. J. Twitchen, B. M. Terhal, and T. H. Taminiau. Fault-tolerant operation of a logical qubit in a diamond quantum processor. *Nature*, 606(7916):884–889, may 2022.

[2] Chris Adambukulam, Hyma Vallabhapurapu, Brett Johnson, Andrea Morello, and Arne Laucht. All Optical Initialisation and Readout and Coherent Population Trapping of a Single Germanium Vacancy in Diamond. *Bulletin of the American Physical Society*, 2023.

[3] Audrius Alkauskas, Bob B. Buckley, David D. Awschalom, and Chris G. Van De Walle. First-principles theory of the luminescence lineshape for the triplet transition in diamond NV centres. *New Journal of Physics*, 16(7):073026, jul 2014.

[4] Jesús Arjona Martínez, Ryan A. Parker, Kevin C. Chen, Carola M. Purser, Linsen Li, Cathryn P. Michaels, Alexander M. Stramma, Romain Debroux, Isaac B. Harris, Martin Hayhurst Appel, Eleanor C. Nichols, Matthew E. Trusheim, Dorian A. Gangloff, Dirk Englund, and Mete Atatüre. Photonic Indistinguishability of the Tin-Vacancy Center in Nanostructured Diamond. *Physical Review Letters*, 129(17):173603, oct 2022.

[5] Serwan Asaad, Vincent Mourik, Benjamin Joecker, Mark A. I. Johnson, Andrew D. Baczewski, Hannes R. Firgau, Mateusz T. Mądzik, Vivien Schmitt, Jarryd J. Pla, Fay E. Hudson, Kohei M. Itoh, Jeffrey C. Mccallum, Andrew S. Dzurak, Arne Laucht, and Andrea Morello. Coherent electrical control of a single high-spin nucleus in silicon. *Nature*, 579(7798):205–209, mar 2019.

[6] Mete Atatüre, Dirk Englund, Nick Vamivakas, Sang Yun Lee, and Joerg Wrachtrup. Material platforms for spin-based photonic quantum technologies. *Nature Reviews Materials*, 3(5):38–51, 2018.

[7] David D. Awschalom, Ronald Hanson, Jörg Wrachtrup, and Brian B. Zhou. Quantum technologies with optically interfaced solid-state spins, sep 2018.

[8] Mohammad Saeed Bahramy, Marcel H.F. Sluiter, and Yoshiyuki Kawazoe. Pseudopotential hyperfine calculations through perturbative core-level po-

larization. *Physical Review B - Condensed Matter and Materials Physics*, 76(3):035124, jul 2007.

[9] Sabyasachi Barik, Aziz Karasahin, Christopher Flower, Tao Cai, Hirokazu Miyake, Wade DeGottardi, Mohammad Hafezi, and Edo Waks. A topological quantum optics interface. *Science*, 359(6376):666–668, 2018.

[10] Sean D. Barrett and Pieter Kok. Efficient high-fidelity quantum computation using matter qubits and linear optics. *Physical Review A - Atomic, Molecular, and Optical Physics*, 71(6):060310, 2005.

[11] Jonas N. Becker, Benjamin Pingault, David Groß, Mustafa Gündoğan, Nadezhda Kukharchyk, Matthew Markham, Andrew Edmonds, Mete Atatüre, Pavel Bushev, and Christoph Becher. All-Optical Control of the Silicon-Vacancy Spin in Diamond at Millikelvin Temperatures. *Physical Review Letters*, 120(5):053603, jan 2018.

[12] M. K. Bhaskar, D. D. Sukachev, A. Sipahigil, R. E. Evans, M. J. Burek, C. T. Nguyen, L. J. Rogers, P. Siyushev, M. H. Metsch, H. Park, F. Jelezko, M. Lončar, and M. D. Lukin. Quantum Nonlinear Optics with a Germanium-Vacancy Color Center in a Nanoscale Diamond Waveguide. *Physical Review Letters*, 118(22):223603, may 2017.

[13] Matthias Bock, Pascal Eich, Stephan Kucera, Matthias Kreis, Andreas Lenhard, Christoph Becher, and Jürgen Eschner. High-fidelity entanglement between a trapped ion and a telecom photon via quantum frequency conversion. *Nature Communications*, 9(1), 2018.

[14] Michel Bockstedte, Felix Schütz, Thomas Garratt, Viktor Ivády, and Adam Gali. Ab initio description of highly correlated states in defects for realizing quantum bits. *npj Quantum Materials*, 3(1):31, dec 2018.

[15] J. J. Bollinger, J. D. Prestage, Wayne M. Itano, and D. J. Wineland. Laser-cooled-atomic frequency standard. *Physical Review Letters*, 54(10):1000–1003, mar 1985.

[16] Alexandre Bourassa, Christopher P. Anderson, Kevin C. Miao, Mykyta Onizhuk, He Ma, Alexander L. Crook, Hiroshi Abe, Jawad Ul-Hassan, Takeshi Ohshima, Nguyen T. Son, Giulia Galli, and David D. Awschalom. Entanglement and control of single nuclear spins in isotopically engineered silicon carbide. *Nature Materials*, 19(12):1319–1325, 2020.

[17] C. E. Bradley, S. W. de Bone, P. F.W. Möller, S. Baier, M. J. Degen, S. J.H. Loenen, H. P. Bartling, M. Markham, D. J. Twitchen, R. Hanson, D. Elkouss, and T. H. Taminiau. Robust quantum-network memory based on spin qubits in isotopically engineered diamond. *npj Quantum Information*, 8(1):1–9, oct 2022.

[18] C. E. Bradley, J. Randall, M. H. Abobeih, R. C. Berrevoets, M. J. Degen, M. A. Bakker, M. Markham, D. J. Twitchen, and T. H. Taminiau. A Ten-Qubit Solid-State Spin Register with Quantum Memory up to One Minute. *Physical Review X*, 9(3), 2019.

[19] C. Cabrillo, J. I. Cirac, P. García-Fernández, P. Zoller, P Garcí A-Ferná Ndez, and P. Zoller. Creation of entangled states of distant atoms by interference. *Physical Review A - Atomic, Molecular, and Optical Physics*, 59(2):1025–1033, 1999.

[20] L. Childress, D. J. Twitchen, B. Hensen, M. S. Blok, L. Robledo, R. Hanson, G. Koolstra, H. Bernien, M. Markham, T. H. Taminiau, and W. Pfaff. Heralded entanglement between solid-state qubits separated by three metres. *Nature*, 497(7447):86–90, apr 2013.

[21] Hyeongrak Choi, Mihir Pant, Saikat Guha, and Dirk Englund. Percolation-based architecture for cluster state creation using photon-mediated entanglement between atomic memories. *npj Quantum Information*, 5(1):1–7, nov 2019.

[22] Y. Chu, N. P. De Leon, B. J. Shields, B. Hausmann, R. Evans, E. Togan, M. J. Burek, M. Markham, A. Stacey, A. S. Zibrov, A. Yacoby, D. J. Twitchen, M. Loncar, H. Park, P. Maletinsky, and M. D. Lukin. Coherent optical transitions in implanted nitrogen vacancy centers. *Nano Letters*, 14(4):1982–1986, 2014.

[23] Christopher J. Ciccarino, Johannes Flick, Isaac B. Harris, Matthew E. Trusheim, Dirk R. Englund, and Prineha Narang. Strong spin–orbit quenching via the product Jahn–Teller effect in neutral group IV qubits in diamond. *npj Quantum Materials*, 5(1):1–6, oct 2020.

[24] Christoph Clausen, Imam Usmani, Félix Bussiéres, Nicolas Sangouard, Mikael Afzelius, Hugues De Riedmatten, and Nicolas Gisin. Quantum storage of photonic entanglement in a crystal. *Nature*, 469(7331):508–512, 2011.

[25] Alexander L. Crook, Christopher P. Anderson, Kevin C. Miao, Alexandre Bourassa, Hope Lee, Sam L. Bayliss, David O. Bracher, Xingyu Zhang, Hiroshi Abe, Takeshi Ohshima, Evelyn L. Hu, and David D. Awschalom. Purcell enhancement of a single silicon carbide color center with coherent spin control. *Nano Letters*, 20(5):3427–3434, may 2020.

[26] Romain Debroux, Cathryn P. Michaels, Carola M. Purser, Noel Wan, Matthew E. Trusheim, Jesús Arjona Martínez, Ryan A. Parker, Alexander M. Stramma, Kevin C. Chen, Lorenzo De Santis, Evgeny M. Alexeev, Andrea C. Ferrari, Dirk Englund, Dorian A. Gangloff, and Mete Atatüre. Quantum Control of the Tin-Vacancy Spin Qubit in Diamond. *Physical Review X*, 11(4):041041, dec 2021.

[27] M. J. Degen, S. J.H. H Loenen, H. P. Bartling, C. E. Bradley, A. L. Meinsma, M. Markham, D. J. Twitchen, and T. H. Taminiau. Entanglement of dark electron-nuclear spin defects in diamond. *Nature Communications*, 12(1), 2021.

[28] Emil V. Denning, Dorian A. Gangloff, Mete Atatüre, Jesper Mørk, and Claire Le Gall. Collective Quantum Memory Activated by a Driven Central Spin. *Physical Review Letters*, 123(14), 2019.

[29] M. W. Doherty, N. B. Manson, P. Delaney, and L. C.L. Hollenberg. The negatively charged nitrogen-vacancy centre in diamond: The electronic solution. *New Journal of Physics*, 13(2):025019, feb 2011.

[30] Erik R. Eisenach, John F. Barry, Michael F. O'Keeffe, Jennifer M. Schloss, Matthew H. Steinecker, Dirk R. Englund, and Danielle A. Braje. Cavity-enhanced microwave readout of a solid-state spin sensor. *Nature Communications*, 12(1):1–7, mar 2021.

[31] E. A. Ekimov, S. G. Lyapin, K. N. Boldyrev, M. V. Kondrin, R. Khmelnitskiy, V. A. Gavva, T. V. Kotereva, and M. N. Popova. Germanium–vacancy color center in isotopically enriched diamonds synthesized at high pressures. *JETP Letters*, 102(11):701–706, dec 2015.

[32] R. E. Evans, M. K. Bhaskar, D. D. Sukachev, C. T. Nguyen, A. Sipahigil, M. J. Burek, B. Machielse, G. H. Zhang, A. S. Zibrov, E. Bielejec, H. Park, M. Lončar, and M. D. Lukin. Photon-mediated interactions between quantum emitters in a diamond nanocavity. *Science*, 362(6415):662–665, 2018.

[33] Christoph Freysoldt, Blazej Grabowski, Tilmann Hickel, Jörg Neugebauer, Georg Kresse, Anderson Janotti, and Chris G de Walle. First-principles calculations for point defects in solids. *Reviews of Modern Physics*, 86(1):253–305, mar 2014.

[34] Ádám Gali. Ab initio theory of the nitrogen-vacancy center in diamond, nov 2019.

[35] Adam Gali and Jeronimo R. Maze. Ab initio study of the split silicon-vacancy defect in diamond: Electronic structure and related properties. *Physical Review B - Condensed Matter and Materials Physics*, 88(23):235205, dec 2013.

[36] P. Giannozzi, O. Andreussi, T. Brumme, O. Bunau, M. Buongiorno Nardelli, M. Calandra, R. Car, C. Cavazzoni, D. Ceresoli, M. Cococcioni, N. Colonna, I. Carnimeo, A. Dal Corso, S. De Gironcoli, P. Delugas, R. A. Distasio, A. Ferretti, A. Floris, G. Fratesi, G. Fugallo, R. Gebauer, U. Gerstmann, F. Giustino, T. Gorni, J. Jia, M. Kawamura, H. Y. Ko, A. Kokalj, E. Kücükbenli, M. Lazzeri, M. Marsili, N. Marzari, F. Mauri, N. L. Nguyen, H. V. Nguyen, A. Otero-De-La-Roza, L. Paulatto, S. Poncé, D. Rocca, R. Sabatini, B. Santra, M. Schlipf, A. P. Seitsonen, A. Smogunov, I. Timrov, T. Thonhauser, P. Umari, N. Vast, X. Wu,

and S. Baroni. Advanced capabilities for materials modelling with Quantum ESPRESSO. *Journal of Physics Condensed Matter*, 29(46):465901, 2017.

[37] Paolo Giannozzi, Stefano Baroni, Nicola Bonini, Matteo Calandra, Roberto Car, Carlo Cavazzoni, Davide Ceresoli, Guido L. Chiarotti, Matteo Cococcioni, Ismaila Dabo, Andrea Dal Corso, Stefano De Gironcoli, Stefano Fabris, Guido Fratesi, Ralph Gebauer, Uwe Gerstmann, Christos Gougoussis, Anton Kokalj, Michele Lazzeri, Layla Martin-Samos, Nicola Marzari, Francesco Mauri, Riccardo Mazzarello, Stefano Paolini, Alfredo Pasquarello, Lorenzo Paulatto, Carlo Sbraccia, Sandro Scandolo, Gabriele Sclauzero, Ari P. Seitsonen, Alexander Smogunov, Paolo Umari, and Renata M. Wentzcovitch. QUANTUM ESPRESSO: A modular and open-source software project for quantum simulations of materials. *Journal of Physics Condensed Matter*, 21(39):395502, 2009.

[38] J. P. Goss, R. Jones, S. J. Breuer, P. R. Briddon, and S. Öberg. The twelve-line 1.682 eV luminescence center in diamond and the vacancy-silicon complex. *Physical Review Letters*, 77(14):3041–3044, sep 1996.

[39] A. Gruber, A. Dräbenstedt, C. Tietz, L. Fleury, J. Wrachtrup, and C. Von Borczyskowski. Scanning confocal optical microscopy and magnetic resonance on single defect centers. *Science*, 276(5321):2012–2014, jun 1997.

[40] Isaac Harris, Christopher J. Ciccarino, Johannes Flick, Dirk R. Englund, and Prineha Narang. Group-III quantum defects in diamond are stable spin-1 color centers. *Physical Review B*, 102(19):195206, nov 2020.

[41] Isaac B. W. Harris, Cathryn P. Michaels, Kevin C. Chen, Ryan A. Parker, Michael Titze, Jesus Arjona Martinez, Madison Sutula, Ian R. Christen, Alexander M. Stramma, William Roth, Carola M. Purser, Martin Hayhurst Appel, Chao Li, Matthew E. Trusheim, Nicola L. Palmer, Matthew L. Markham, Edward S. Bielejec, Mete Atature, and Dirk Englund. Hyperfine Spectroscopy of Isotopically Engineered Group-IV Color Centers in Diamond. *Pre-print*, 2023.

[42] Christian Hepp. *Electronic Structure of the Silicon Vacancy Color Center in Diamond*. PhD thesis, Universität des Saarlandes, 2014.

[43] Christian Hepp, Tina Müller, Victor Waselowski, Jonas N. Becker, Benjamin Pingault, Hadwig Sternschulte, Doris Steinmüller-Nethl, Adam Gali, Jeronimo R. Maze, Mete Atatüre, and Christoph Becher. Electronic structure of the silicon vacancy color center in diamond. *Physical Review Letters*, 112(3):036405, jan 2014.

[44] Daniel B Higginbottom, Alexander T.K. Kurkjian, Camille Chartrand, Moein Kazemi, Nicholas A Brunelle, Evan R. MacQuarrie, James R Klein, Nicholas R Lee-Hone, Jakub Stacho, Myles Ruether, Camille Bowness, Laurent Bergeron, Adam DeAbreu, Stephen R Harrigan, Joshua Kanaganayagam, Danica W

Marsden, Timothy S Richards, Leea A Stott, Sjoerd Roorda, Kevin J Morse, Michael L.W. Thewalt, and Stephanie Simmons. Optical observation of single spins in silicon. *Nature*, 607(7918):266–270, 2022.

[45] Julian Hofmann, Michael Krug, Norbert Ortegel, Lea Gérard, Markus Weber, Wenjamin Rosenfeld, and Harald Weinfurter. Heralded entanglement between widely separated atoms. *Science*, 336(6090):72–75, 2012.

[46] P. Hohenberg and W. Kohn. Inhomogeneous electron gas. *Physical Review*, 136(3B):B864–B871, nov 1964.

[47] D. Hucul, I. V. Inlek, G. Vittorini, C. Crocker, S. Debnath, S. M. Clark, and C. Monroe. Modular entanglement of atomic qubits using photons and phonons. *Nature Physics*, 11(1):37–42, nov 2015.

[48] Peter C Humphreys, Norbert Kalb, Jaco P.J. Morits, Raymond N Schouten, Raymond F.L. Vermeulen, Daniel J Twitchen, Matthew Markham, and Ronald Hanson. Deterministic delivery of remote entanglement on a quantum network. *Nature*, 558(7709):268–273, 2018.

[49] I. V. Inlek, C. Crocker, M. Lichtman, K. Sosnova, and C. Monroe. Multispecies Trapped-Ion Node for Quantum Networking. *Physical Review Letters*, 118(25), 2017.

[50] Toshiro Inubushi, Norikazu Mizuochi, Fumitaka Ishibashi, Mutsuko Hatano, Yuki Doi, Yoshiyuki Miyamoto, Lachlan J. Rogers, Satoshi Kobayashi, Satoshi Yamasaki, Fedor Jelezko, Shinji Nagamachi, Boris Naydenov, Kosuke Tahara, Kay D. Jahnke, Takayuki Iwasaki, and Takehide Miyazaki. Germanium-Vacancy Single Color Centers in Diamond. *Scientific Reports*, 5(1):12882, oct 2015.

[51] Takayuki Iwasaki, Yoshiyuki Miyamoto, Takashi Taniguchi, Petr Siyushev, Mathias H. Metsch, Fedor Jelezko, and Mutsuko Hatano. Tin-Vacancy Quantum Emitters in Diamond. *Physical Review Letters*, 119(25):253601, dec 2017.

[52] H. A. Jahn and E. Teller. Stability of polyatomic molecules in degenerate electronic states - I—Orbital degeneracy. *Proceedings of the Royal Society of London. Series A - Mathematical and Physical Sciences*, 161(905):220–235, jul 1937.

[53] Kay D. Jahnke, Alp Sipahigil, Jan M. Binder, Marcus W. Doherty, Mathias Metsch, Lachlan J. Rogers, Neil B. Manson, Mikhail D. Lukin, and Fedor Jelezko. Electron-phonon processes of the silicon-vacancy centre in diamond. *New Journal of Physics*, 17(4):043011, apr 2015.

[54] N. Kalb, A. A. Reiserer, P. C. Humphreys, J. J.W. Bakermans, S. J. Kamerling, N. H. Nickerson, S. C. Benjamin, D. J. Twitchen, M. Markham, and R. Hanson. Entanglement distillation between solid-state quantum network nodes. *Science*, 356(6341):928–932, jun 2017.

[55] Donggyu Kim, Mohamed I. Ibrahim, Christopher Foy, Matthew E. Trusheim, Ruonan Han, and Dirk R. Englund. A CMOS-integrated quantum sensor based on nitrogen–vacancy centres. *Nature Electronics*, 2(7):284–289, jul 2019.

[56] Jonathan M. Kindem, Andrei Ruskuc, John G. Bartholomew, Jake Rochman, Yan Qi Huan, and Andrei Faraon. Control and single-shot readout of an ion embedded in a nanophotonic cavity. *Nature*, 580(7802):201–204, mar 2020.

[57] W. Kohn and L. J. Sham. Self-consistent equations including exchange and correlation effects. *Physical Review*, 140(4A):A1133–A1138, nov 1965.

[58] Rodrick Kuate Defo, Efthimios Kaxiras, and Steven L Richardson. Calculating the hyperfine tensors for group-IV impurity-vacancy centers in diamond using hybrid density functional theory. *Physical Review B*, 104(7):75158, 2021.

[59] B. MacHielse, S. Bogdanovic, S. Meesala, S. Gauthier, M. J. Burek, G. Joe, M. Chalupnik, Y. I. Sohn, J. Holzgrafe, R. E. Evans, C. Chia, H. Atikian, M. K. Bhaskar, D. D. Sukachev, L. Shao, S. Maity, M. D. Lukin, and M. Lončar. Quantum Interference of Electromechanically Stabilized Emitters in Nanophotonic Devices. *Physical Review X*, 9(3):031022, aug 2019.

[60] Smarak Maity, Linbo Shao, Young Ik Sohn, Srujan Meesala, Bartholomeus Machielse, Edward Bielejec, Matthew Markham, and Marko Lončar. Spectral Alignment of Single-Photon Emitters in Diamond using Strain Gradient. *Physical Review Applied*, 10(2):024050, aug 2018.

[61] Srujan Meesala, Young Ik Sohn, Benjamin Pingault, Linbo Shao, Haig A Atikian, Jeffrey Holzgrafe, Mustafa Gündoğan, Camille Stavrakas, Alp Sipahigil, Cleaven Chia, Ruffin Evans, Michael J Burek, Mian Zhang, Lue Wu, Jose L Pacheco, John Abraham, Edward Bielejec, Mikhail D Lukin, Mete Atatüre, and Marko Lončar. Strain engineering of the silicon-vacancy center in diamond. *Physical Review B*, 97(20):205444, 2018.

[62] Cathryn P. Michaels, Jesus Arjona Martinez, Romain Debroux, Ryan A. Parker, Alexander M. Stramma, Luca I. Huber, Carola M. Purser, Mete Atature, and Dorian A. Gangloff. Multidimensional cluster states using a single spin-photon interface coupled strongly to an intrinsic nuclear register. *Quantum*, 5:565, 2021.

[63] Sara Mouradian, Noel H. Wan, Tim Schröder, and Dirk Englund. Rectangular photonic crystal nanobeam cavities in bulk diamond. *Applied Physics Letters*, 111(2):021103, jul 2017.

[64] Sara L. Mouradian, Tim Schröder, Carl B. Poitras, Luozhou Li, Jordan Goldstein, Edward H. Chen, Michael Walsh, Jaime Cardenas, Matthew L. Markham, Daniel J. Twitchen, Michal Lipson, and Dirk Englund. Scalable Integration of Long-Lived Quantum Memories into a Photonic Circuit. *Physical Review X*, 5(3):031009, jul 2015.

[65] Markéta L. Munzarová. DFT Calculations of EPR Hyperfine Coupling Tensors. In *Calculation of NMR and EPR Parameters*, pages 461–482. Wiley-VCH Verlag GmbH & Co. KGaA, may 2004.

[66] Elke Neu, Christian Hepp, Michael Hauschild, Stefan Gsell, Martin Fischer, Hadwig Sternschulte, Doris Steinmüller-Nethl, Matthias Schreck, and Christoph Becher. Low-temperature investigations of single silicon vacancy colour centres in diamond. *New Journal of Physics*, 15(4):43005, 2013.

[67] Tomáš Neuman, Matt Eichenfield, Matthew E. Trusheim, Lisa Hackett, Prineha Narang, and Dirk Englund. A phononic interface between a superconducting quantum processor and quantum networked spin memories. *npj Quantum Information*, 7(1):1–8, aug 2021.

[68] C T Nguyen, D D Sukachev, M K Bhaskar, B. MacHielse, D S Levonian, E N Knall, P Stroganov, C Chia, M J Burek, R Riedinger, H Park, M Lončar, and M D Lukin. An integrated nanophotonic quantum register based on silicon-vacancy spins in diamond. *Physical Review B*, 100(16):165428, 2019.

[69] C. T. Nguyen, D. D. Sukachev, M. K. Bhaskar, B. Machielse, D. S. Levonian, E. N. Knall, P. Stroganov, R. Riedinger, H. Park, M. Lončar, and M. D. Lukin. Quantum Network Nodes Based on Diamond Qubits with an Efficient Nanophotonic Interface. *Physical Review Letters*, 123(18):183602, oct 2019.

[70] Naomi H. Nickerson, Ying Li, and Simon C. Benjamin. Topological quantum computing with a very noisy network and local error rates approaching one percent. *Nature Communications*, 4, 2013.

[71] Mykyta Onizhuk, Kevin C Miao, Joseph P Blanton, He Ma, Christopher P Anderson, Alexandre Bourassa, David D Awschalom, and Giulia Galli. Probing the Coherence of Solid-State Qubits at Avoided Crossings. *PRX Quantum*, 2(1):10311, 2021.

[72] Ryan A. Parker, Jesús Arjona Martínez, Kevin C. Chen, Alexander M Stramma, Isaac B. Harris, Cathryn P. Michaels, Matthew E. Trusheim, Martin Hayhurst Appel, Carola M. Purser, William G Roth, Dirk R. Englund, Mete Atatüre, Jesús Arjona Martínez, Kevin C. Chen, Alex Strammer, Isaac B. Harris, Cathryn P. Michaels, Matthew E. Trusheim, Carola M. Purser, Martin Hayhurst Appel, Dirk R. Englund, and Mete Atatüre. A diamond nanophotonic interface with an optically accessible deterministic electronuclear spin register. *Pre-print*, 2023.

[73] John P Perdew, Kieron Burke, and Matthias Ernzerhof. Generalized Gradient Approximation Made Simple. *Physical Review Letters*, 77(18):3865–3868, oct 1996.

[74] Wolfgang Pfaff, Tim H. Taminiau, Lucio Robledo, Hannes Bernien, Matthew Markham, Daniel J. Twitchen, and Ronald Hanson. Demonstration of

entanglement-by-measurement of solid-state qubits. *Nature Physics*, 9(1):29–33, oct 2013.

[75] Chris J Pickard and Francesco Mauri. All-electron magnetic response with pseudopotentials: NMR chemical shifts. *Physical Review B*, 63(24):245101, may 2001.

[76] Benjamin Pingault, David Dominik Jarausch, Christian Hepp, Lina Klintberg, Jonas N. Becker, Matthew Markham, Christoph Becher, and Mete Atatüre. Coherent control of the silicon-vacancy spin in diamond. *Nature Communications*, 8(1):1–7, may 2017.

[77] M. Pompili, S. L.N. N Hermans, S. Baier, H. K.C. C Beukers, P. C. Humphreys, R. N. Schouten, R. F.L. L Vermeulen, M. J. Tiggelman, L Dos, Santos Martins, B. Dirkse, S. Wehner, R. Hanson, L. dos Santos Martins, B. Dirkse, S. Wehner, and R. Hanson. Realization of a multinode quantum network of remote solid-state qubits. *Science*, 372(6539):259–264, apr 2021.

[78] Mihika Prabhu, Carlos Errando-Herranz, Lorenzo De Santis, Ian Christen, Changchen Chen, Connor Gerlach, and Dirk Englund. Individually addressable and spectrally programmable artificial atoms in silicon photonics. *Nature Communications*, 14(1):1–7, apr 2023.

[79] Hamza Raniwala, Stefan Krastanov, Lisa Hackett, Matt Eichenfield, Dirk R Englund, and Matthew E Trusheim. Spin-Phonon-Photon Strong Coupling in a Piezomechanical Nanocavity. *Pre-print*, 2022.

[80] Terry Renner, E Richard Cohen;, and Tom Cvitas; Jeremy G Frey; Bertil Holström; Kozo Kuchitsu; Roberto Marquardt; Ian Mills; Franco Pavese; Martin Quack; Jüergen Stohner; Herbert L Strauss; Michio Takami; Anders J Thor. *Quantities, Units and Symbols in Physical Chemistry*. Royal Society of Chemistry, 2007.

[81] Stephan Ritter, Christian Nölleke, Carolin Hahn, Andreas Reiserer, Andreas Neuzner, Manuel Uphoff, Martin Mücke, Eden Figueroa, Joerg Bochmann, and Gerhard Rempe. An elementary quantum network of single atoms in optical cavities. *Nature*, 484(7393):195–200, 2012.

[82] Lachlan J Rogers, Kay D Jahnke, Mathias H Metsch, Alp Sipahigil, Jan M Binder, Tokuyuki Teraji, Hitoshi Sumiya, Junichi Isoya, Mikhail D Lukin, Philip Hemmer, and Fedor Jelezko. All-optical initialization, readout, and coherent preparation of single silicon-vacancy spins in diamond. *Physical Review Letters*, 113(26):263602, 2014.

[83] Andrei Ruskuc, Chun Ju Wu, Jake Rochman, Joonhee Choi, and Andrei Faraon. Nuclear spin-wave quantum register for a solid-state qubit. *Nature*, 602(7897):408–413, feb 2022.

[84] A Sipahigil, K D Jahnke, L J Rogers, T Teraji, J Isoya, A S Zibrov, F Jelezko, and M D Lukin. Indistinguishable photons from separated silicon-vacancy centers in diamond. *Physical Review Letters*, 113(11):113602, 2014.

[85] P.-J. Stas, Y. Q. Huan, B. Machielse, E. N. Knall, A. Suleymanzade, B. Pingault, M. Sutula, S. W. Ding, C. M. Knaut, D. R. Assumpcao, Y.-C. Wei, M. K. Bhaskar, R. Riedinger, D. D. Sukachev, H. Park, M. Lončar, D. S. Levonian, and M. D. Lukin. Robust multi-qubit quantum network node with integrated error detection. *Science*, 378(6619):557–560, nov 2022.

[86] T. Staudacher, F. Shi, S. Pezzagna, J. Meijer, J. Du, C. A. Meriles, F. Reinhard, and J. Wrachtrup. Nuclear magnetic resonance spectroscopy on a (5-nanometer)3 sample volume. *Science*, 339(6119):561–563, feb 2013.

[87] D. D. Sukachev, A. Sipahigil, C. T. Nguyen, M. K. Bhaskar, R. E. Evans, F. Jelezko, and M. D. Lukin. Silicon-Vacancy Spin Qubit in Diamond: A Quantum Memory Exceeding 10 ms with Single-Shot State Readout. *Physical Review Letters*, 119(22):223602, nov 2017.

[88] Madison Sutula, Ian Christen, Eric Bersin, Michael P Walsh, Kevin C Chen, Justin Mallek, Alexander Melville, Michael Titze, Edward S Bielejec, Scott Hamilton, Danielle Braje, P. Benjamin Dixon, and Dirk R Englund. Large-scale optical characterization of solid-state quantum emitters. *Pre-print*, 2022.

[89] Krisztián Szász, Tamás Hornos, Martijn Marsman, and Adam Gali. Hyperfine coupling of point defects in semiconductors by hybrid density functional calculations: The role of core spin polarization. *Physical Review B - Condensed Matter and Materials Physics*, 88(7):75202, 2013.

[90] Gergo Thiering and Adam Gali. Theory of the optical spin-polarization loop of the nitrogen-vacancy center in diamond. *Physical Review B*, 98(8):85207, aug 2018.

[91] Gergő Thiering and Adam Gali. The (eg $\otimes$ eu) $\otimes$ Eg product Jahn–Teller effect in the neutral group-IV vacancy quantum bits in diamond. *npj Computational Materials*, 5(1):18, dec 2019.

[92] Gergő Gergó Thiering and Adam Gali. Ab Initio Magneto-Optical Spectrum of Group-IV Vacancy Color Centers in Diamond. *Physical Review X*, 8(2):21063, jun 2018.

[93] Michael Tinkham. *Group theory and quantum mechanics*. Dover Publications, 1992.

[94] Matthew E. Trusheim, Benjamin Pingault, Noel H. Wan, Mustafa Gündoğan, Lorenzo De Santis, Romain Debroux, Dorian Gangloff, Carola Purser, Kevin C. Chen, Michael Walsh, Joshua J. Rose, Jonas N. Becker, Benjamin Lienhard,

Eric Bersin, Ioannis Paradeisanos, Gang Wang, Dominika Lyzwa, Alejandro R.P. Montblanch, Girish Malladi, Hassaram Bakhru, Andrea C. Ferrari, Ian A. Walmsley, Mete Atatüre, and Dirk Englund. Transform-Limited Photons from a Coherent Tin-Vacancy Spin in Diamond. *Physical Review Letters*, 124(2), 2020.

[95] Péter Udvarhelyi, Bálint Somogyi, Gergo Thiering, and Adam Gali. Identification of a Telecom Wavelength Single Photon Emitter in Silicon. *Physical Review Letters*, 127(19), 2021.

[96] S B Van Dam, M Walsh, M J Degen, E Bersin, S L Mouradian, A Galiullin, M Ruf, M Ijspeert, T H Taminiau, R Hanson, and D R Englund. Optical coherence of diamond nitrogen-vacancy centers formed by ion implantation and annealing. *Physical Review B*, 99(16), 2019.

[97] Chris G. Van De Walle, D. B. Laks, G. F. Neumark, S. T. Pantelides, and P. E. Blöchl. First-principles calculations of solubilities and doping limits: Li, Na, and N in ZnSe. *Physical Review B*, 47(15):9425–9434, 1993.

[98] Noel H. Wan, Tsung Ju Lu, Kevin C. Chen, Michael P. Walsh, Matthew E. Trusheim, Lorenzo De Santis, Eric A. Bersin, Isaac B. Harris, Sara L. Mouradian, Ian R. Christen, Edward S. Bielejec, and Dirk Englund. Large-scale integration of artificial atoms in hybrid photonic circuits. *Nature*, 583(7815):226–231, jul 2020.

[99] Hanfeng Wang, Matthew E. Trusheim, Laura Kim, Hamza Raniwala, and Dirk R. Englund. Field programmable spin arrays for scalable quantum repeaters. *Nature Communications*, 14(1), 2023.

[100] Peng Wang, Takashi Taniguchi, Yoshiyuki Miyamoto, Mutsuko Hatano, and Takayuki Iwasaki. Low-Temperature Spectroscopic Investigation of Lead-Vacancy Centers in Diamond Fabricated by High-Pressure and High-Temperature Treatment. *ACS Photonics*, 8(10):2947–2954, oct 2021.

[101] Yong Yu, Fei Ma, Xi Yu Luo, Bo Jing, Peng Fei Sun, Ren Zhou Fang, Chao Wei Yang, Hui Liu, Ming Yang Zheng, Xiu Ping Xie, Wei Jun Zhang, Li Xing You, Zhen Wang, Teng Yun Chen, Qiang Zhang, Xiao Hui Bao, and Jian Wei Pan. Entanglement of two quantum memories via fibres over dozens of kilometres. *Nature*, 578(7794):240–245, 2020.

[102] Tian Zhong, Jonathan M. Kindem, John G. Bartholomew, Jake Rochman, Ioana Craiciu, Varun Verma, Sae Woo Nam, Francesco Marsili, Matthew D. Shaw, Andrew D. Beyer, and Andrei Faraon. Optically Addressing Single Rare-Earth Ions in a Nanophotonic Cavity. *Physical Review Letters*, 121(18), 2018.

[103] J F Ziegler, J P Biersack, and M D Ziegler. SRIM, the stopping and range of ions in matter. *Nuclear Instruments and Methods in Physics Research Section B: Beam Interactions with Materials and Atoms*, 268(11-12):1818–1823, 2008.